

Clustering dark energy imprints on cosmological observables of the gravitational field

Farbod Hassani ^{1*}, Julian Adamek ^{2,†} and Martin Kunz ^{1,‡}

¹Département de Physique Théorique, Université de Genève, 24 quai Ernest Ansermet, 1211 Genève 4, Switzerland

²School of Physics and Astronomy, Queen Mary University of London, 327 Mile End Road, London E1 4NS, UK

Accepted XXX. Received YYY; in original form ZZZ

ABSTRACT

We study cosmological observables on the past light cone of a fixed observer in the context of clustering dark energy. We focus on observables that probe the gravitational field directly, namely the integrated Sachs-Wolfe and non-linear Rees-Sciama effect (ISW-RS), weak gravitational lensing, gravitational redshift and Shapiro time delay. With our purpose-built N -body code “ k -evolution” that tracks the coupled evolution of dark matter particles and the dark energy field, we are able to study the regime of low speed of sound c_s where dark energy perturbations can become quite large. Using ray tracing we produce two-dimensional sky maps for each effect and we compute their angular power spectra. It turns out that the ISW-RS signal is the most promising probe to constrain clustering dark energy properties coded in $w - c_s^2$, as the *linear* clustering of dark energy would change the angular power spectrum by $\sim 30\%$ at low ℓ when comparing two different speeds of sound for dark energy. Weak gravitational lensing, Shapiro time-delay and gravitational redshift are less sensitive probes of clustering dark energy, showing variations of a few percent only. The effect of dark energy *non-linearities* in all the power spectra is negligible at low ℓ , but reaches about 2% and 3%, respectively, in the convergence and ISW-RS angular power spectra at multipoles of a few hundred when observed at redshift ~ 0.85 . Future cosmological surveys achieving percent precision measurements will allow to probe the clustering of dark energy to a high degree of confidence. Clear evidence for clustering dark energy at any scale would rule out a cosmological constant as the leading contender for dark energy, and may help to distinguish between different dark energy models.

Key words: dark energy – large-scale structure of the Universe – N -body simulations

1 INTRODUCTION

The accelerated expansion of the Universe which has been attributed to the so called “dark energy” component was first discovered using supernova Ia observations over two decades ago independently by [Perlmutter et al. \(1999\)](#) and [Riess et al. \(1998\)](#). Since then the late-time accelerating expansion has been confirmed by several independent measurements, including the cosmic microwave background (CMB) ([Ade et al. 2016b](#); [Spergel et al. 2003](#); [Ade et al. 2016a](#)), large scale structure ([Tegmark et al. 2004, 2006](#)) and baryon acoustic oscillations ([Aubourg et al. 2015](#); [Percival et al. 2007](#)).

In the Λ CDM standard model of cosmology the cosmological constant Λ is responsible for the late-time accel-

eration. Although Λ CDM is a successful model that fits the current data well, Λ is a phenomenological parameter which is not theoretically well motivated and suffers from severe fundamental issues including fine-tuning of the initial energy density and the coincidence problem [see [Martin \(2012\)](#) for a review of the cosmological constant problem]. The theoretical issues of the cosmological constant and tensions between some parameters in various cosmological data sets ([Handley & Lemos 2019](#); [Verde et al. 2019](#)) that have emerged over the past years have motivated cosmologists to propose a plethora of dark energy (in the form of an additional scalar field or “dark” fluid) and modified gravity models (in the form of a modification of general relativity) to explain the late-time cosmic acceleration ([Clifton et al. 2012](#); [Joyce et al. 2016](#); [Koyama 2018](#)). Since the number of viable dark energy and modified gravity models is substantial, the effective field theory (EFT) approach has been developed and has become popular. It describes the theory economically in the low en-

* E-mail: Farbod.Hassani@unige.ch

† E-mail: julian.adamek@qmul.ac.uk

‡ E-mail: martin.kunz@unige.ch

ergy limit using symmetries and can connect the specific theory to the observation in a straightforward way.

In the near future with high precision cosmological surveys such as Euclid (Laureijs et al. 2011), the Dark Energy Spectroscopic Instrument (DESI) (Aghamousa et al. 2016), the Legacy Survey of Space and Time (LSST) (Abate et al. 2012) and the Square Kilometre Array (SKA) (Santos et al. 2015) we will be able to probe the cosmological models with percent precision into the highly nonlinear regime. One of the main goals of these surveys is to understand the reason behind the cosmic acceleration and to probe the nature of gravity. In the case where the data prefers an alternative dark energy scenario, accurate modeling of the cosmological observables for non-standard models up to highly nonlinear scales is required. A very accurate method to model the cosmological predictions of these theories on such scales is obtained using cosmological N -body simulations.

Until now several N -body codes have been developed for a range of alternative gravity models (Oyaizu et al. 2008; Schmidt et al. 2009; Zhao et al. 2011; Li et al. 2012; Brax et al. 2012; Baldi 2012; Puchwein et al. 2013; Wyman et al. 2013; Barreira et al. 2013; Li et al. 2013; Llinares et al. 2014; Mead et al. 2015; Valogiannis & Bean 2017). These codes are based on Newtonian gravity which is not naturally suited for considering the non-standard dark energy models, therefore requiring a number of approximations. While these may be justified for a crude analysis, the fact that dark energy (as opposed to dark matter) is not dominated by rest-mass density appeals more to a relativistic treatment.

With such applications in mind, some of us have developed *gevolution* (Adamek et al. 2016a), an N -body code entirely based on General Relativity (GR). One of the main advantages of the *gevolution* scheme is that it could be extended naturally to include dark energy or modified gravity models without requiring any approximations in the dark energy sector such as the quasi-static approximation as is done in the Newtonian approaches. A full implementation of the EFT of dark energy encompassing many dark energy and modified gravity models is still a formidable task. As a first step toward this goal we have recently developed the k -evolution code in Hassani et al. (2019) in which we have added a k -essence scalar field using the EFT language. Based on *gevolution* some of us have recently also developed N -body simulations for parametrised modified gravity in Hassani & Lombriser (2020), and Reverberi & Daverio (2019) have implemented $f(R)$ models in *gevolution*.

In this article, we study the effect of k -essence dark energy on the cosmological observables of the gravitational field using our N -body codes *gevolution* and k -evolution. In particular, weak gravitational lensing and the ISW-RS effect probe the gravitational potential and its time derivative directly, and they can be constrained with multiple probes independently. We additionally discuss gravitational redshift and the Shapiro time delay, even though their cosmological detection will be more challenging. We study and quantify the signatures that the k -essence model would imprint on each observable.

In Section 2 we discuss the theoretical background, focusing on k -essence in the EFT framework of dark energy, and we present the relevant equations that are solved in k -evolution to evolve the k -essence field. Section 3 is devoted to the general discussion about the cosmological observables

and how non-standard dark energy or modified gravity models would affect each observable. The cosmological parameters of our simulations and the way we construct the past light cone for a fixed observer in our N -body codes to make the synthetic sky maps of our observables are explained in Section 4. In Section 5 we show the numerical results from k -evolution and *gevolution* and we compare the results with the linear theory prediction obtained from the Boltzmann code CLASS. Our conclusions and main take-home points are summarised in Section 6.

2 THEORY

In this section we briefly review the essentials of the k -essence model especially with the focus on its effective field theory description and the k -evolution code, an N -body code recently developed to study the evolution of large scale structure in the presence of a non-linear k -essence scalar field, see Hassani et al. (2019) for a description.

To study the evolution of the perturbations around a homogenous flat Friedmann Universe, we consider the Friedmann-Lemaître-Robertson-Walker (FLRW) metric written in the conformal Poisson gauge,

$$ds^2 = a^2(\tau) \left[-e^{2\Psi} d\tau^2 - 2B_i dx^i d\tau + (e^{-2\Phi} \delta_{ij} + h_{ij}) dx^i dx^j \right], \quad (1)$$

where Ψ and Φ are the Bardeen potentials carrying the scalar perturbations of the metric, B_i is the gravitomagnetic vector perturbation with two degrees of freedom as we have $\delta^{ij} \partial_j B_i = 0$, and h_{ij} is the tensor perturbation with the gauge condition $\delta^{ij} h_{ij} = 0 = \delta^{ij} \partial_i h_{jk}$ which results in two remaining degrees of freedom.

The k -essence model was originally introduced to naturally explain the recent accelerated expansion of the Universe through the idea of a dynamical attractor solution in which this model acts as a cosmological constant at the beginning of the matter dominated era without any fine tuning of the parameters (Armendariz-Picon et al. 2000, 2001). This model is particularly interesting as it does not rely on coincidence or anthropic reasoning, unlike the cosmological constant and quintessence models¹ in which the energy density today is set by tuning the model parameters.

The k -essence action, an action containing at most one single derivative acting on the field, reads

$$S_{\text{DE}} = \int \sqrt{-g} P(X, \varphi) d^4x, \quad (2)$$

where φ is the scalar field and $X = -\frac{1}{2} g^{\mu\nu} \partial_\mu \varphi \partial_\nu \varphi$ is the kinetic term of the k -essence field. In general we need to choose a specific form for the function $P(X, \varphi)$ to solve the equations of motion for the k -essence scalar field. Since there are many possible choices, one can instead employ the EFT approach to model the dynamics of dark energy. EFT, although not a fundamental theory, offers several advantages: First, we can express a large class of dark energy and modified gravity (DE/MG) models with a minimal number of

¹ The quintessence model is a canonical scalar field model, corresponding to the special case of the k -essence model where the kinetic term is canonical.

parameters in a model-independent approach and using a unified language. Second, the phenomenological parameters of the effective theory can be constrained directly by cosmological observations without being specific to any DE/MG models nor to their original motivations. Third, the effective approach allows the theorists to carefully examine the unexplored regions of the space of parameters which could in principle guide towards new viable models (Gubitosi et al. 2013; Creminelli et al. 2009).

In *k*-evolution (Hassani et al. 2019), which is an extension of *gevolution* (Adamek et al. 2016b,a) in which we have implemented the *k*-essence model as a dark energy sector, we use the EFT approach to write down the equations of motion parametrised with the equation of state w and the squared speed of sound c_s^2 . The scalar field evolution, keeping only linear terms of the scalar field and its time derivative, is given by

$$\pi' = \zeta - \mathcal{H}\pi + \Psi, \quad (3)$$

$$\zeta' = 3w\mathcal{H}\zeta - 3c_s^2(\mathcal{H}^2\pi - \mathcal{H}\Psi - \mathcal{H}'\pi - \Phi') + c_s^2\nabla^2\pi, \quad (4)$$

where π is the scalar field perturbation around its background value, ζ is written in terms of π and π' , $\nabla^2 = \delta^{ij}\partial_i\partial_j$, a prime $'$ denotes the time derivative with respect to the conformal time, and \mathcal{H} is the conformal Hubble function. The linear stress energy tensor reads

$$\begin{aligned} T_0^0 &= -\rho + \frac{\rho + p}{c_s^2}(3c_s^2\mathcal{H}\pi - \zeta), \\ T_i^0 &= -(\rho + p)\partial_i\pi, \\ T_j^i &= p\delta_j^i - (\rho + p)(3w\mathcal{H}\pi - \zeta)\delta_j^i. \end{aligned} \quad (5)$$

It is worth noting that in connection with the EFT language, with the notation used in Gleyzes et al. (2013), apart from the background parameters $\Lambda(t)$ and $c(t)$ the only remaining parameter in EFT for *k*-essence theory is $M_2^4(t)$. In the alternative EFT notation using $\alpha_i(t)$ explained in Bellini & Sawicki (2014), α_K is the only non-zero parameter.

As discussed in Hassani et al. (2019), although we keep only linear terms in the scalar field dynamics and we drop higher order self-interactions of π , the scalar field does cluster and form non-linear scalar field structures in *k*-evolution because it is sourced by non-linearities in matter through gravitational coupling. This is the crucial improvement over the treatment of dark energy in *gevolution*, which uses the transfer functions from linear theory to keep track of perturbations in the dark energy fluid similar to how it is done in Dakin et al. (2019) [see also Brando et al. (2020) for a more comprehensive extension of this framework to EFT].

Einstein's equations for the evolution of the scalar perturbations in the weak field regime (Adamek et al. 2017a) read

$$(1 + 2\Phi)\nabla^2\Phi - 3\mathcal{H}\Phi' - 3\mathcal{H}^2\Psi - \frac{1}{2}\delta^{ij}\partial_i\Phi\partial_j\Phi = -4\pi G a^2 \delta T_0^0, \quad (6)$$

$$\begin{aligned} \nabla^4(\Phi - \Psi) - \left(3\delta^{ik}\delta^{jl}\frac{\partial^2}{\partial x^k\partial x^l} - \delta^{ij}\nabla^2\right)\partial_i\Phi\partial_j\Phi \\ = 4\pi G a^2 \left(3\delta^{ik}\frac{\partial^2}{\partial x^j\partial x^k} - \delta_j^i\nabla^2\right)T_i^j, \end{aligned} \quad (7)$$

where the stress tensor T_μ^ν includes all the relevant species, i.e. matter, dark energy and radiation.

In Hassani et al. (2019), we introduce *k*-evolution and the full non-linear equations for the *k*-essence model written using the EFT action. We study the dark energy clustering and its impact on the large scale structure of the Universe. Moreover, we discuss that the scalar dark energy does not lead to significantly larger vector and tensor perturbations than Λ CDM. Thus one can safely neglect the vector and tensor perturbation in this theory. In Hassani et al. (2020) we quantify the non-linear effects from *k*-essence dark energy through the effective parameter $\mu(k, z)$ that encodes the contribution of a dark energy sector to the Poisson equation (see below). We also show that for the *k*-essence model the difference between the two potentials $\Phi - \Psi$ and short-wave corrections appearing as higher order terms in the Poisson equation can be safely neglected. Moreover, in Hansen et al. (2020), we study the effect of *k*-essence dark energy as well as some other modified gravity theories on the turn-around radius — the radius at which the inward velocity due to the gravitational attraction and outward velocity due to the expansion of the Universe cancel each other — in galaxy clusters.

It is sometimes useful to parametrise the effect that clustering dark energy has on the gravitational potential phenomenologically through a modified Poisson equation,

$$-k^2\Phi = 4\pi G_N a^2 \mu(k, z) \sum_X \bar{\rho}_X \Delta_X, \quad (8)$$

where Δ is the comoving density contrast and the species X do not include the dark energy field. Denoting in addition the ratio between the two Bardeen potentials as

$$\eta(k, z) = \frac{\Psi(k, z)}{\Phi(k, z)}, \quad (9)$$

one obtains a phenomenological classification of DE/MG models through two generic functions of time and scale, with Λ CDM predicting $\eta = \mu = 1$ everywhere (e.g. Ade et al. 2016b; Blanchard et al. 2019). As discussed in Hassani et al. (2020), for the case where *k*-essence plays the role of dark energy, $\eta(k, z) \approx 1$ and $\mu(k, z)$ is fitted well with a tanh function where the amplitude and shape of the function depends on the speed of sound and equation of state.

For the sake of completeness, we show the effect of *k*-essence, expressed in the form of $w - c_s^2$ in the parameter space, on the background evolution and the growth of matter density perturbation. The effect of *k*-essence appears on the background evolution via the equation of state but independent of the speed of sound of dark energy. We show the conformal Hubble parameter \mathcal{H} as well as the redshift-distance relation in Fig. 1 in the left and middle panel for w CDM with $w = -0.9$ and Λ CDM, which are the cases we consider in this article. We also compare the logarithmic growth rate $f = d \ln \Delta_m / d \ln a$ in the right panel of Fig. 1 for different scenarios to see the impact of different choices of w and c_s^2 on the growth of structures. The logarithmic growth rate provides a useful way to distinguish between DE/MG gravity and Λ CDM (Kunz & Sapone 2007; Amendola et al. 2018; Dossett & Ishak 2013; Blanchard et al. 2019).

Since the logarithmic growth rate is in general scale dependent, we compute it for different scales by studying the evolution of the comoving matter density contrast Δ_m ,

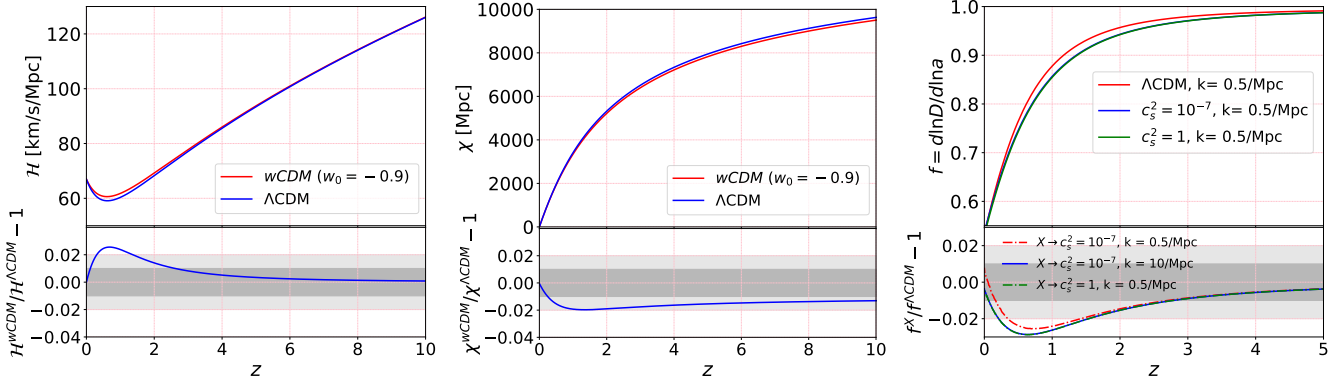


Figure 1. *Left:* The conformal Hubble parameter as a function of redshift for Λ CDM and w CDM with $w_0 = -0.9$. In the bottom panel we show the relative difference. As expected, the effect of dark energy goes away at high redshifts. *Centre:* The comoving distance as a function of redshift for the two cosmologies is plotted. In the bottom panel again the relative difference is shown. The relative difference asymptotes to a constant at high redshifts because the comoving distance is an integrated quantity. *Right:* In the top panel, the logarithmic growth rate f as a function of redshift for a fixed wavenumber is plotted. In the bottom the relative difference between different scenarios is shown with respect to Λ CDM. While in the latter case the growth rate is scale independent (neglecting corrections due to neutrinos), in a clustering dark energy model the behaviour of a mode depends on whether it is inside or outside of the sound horizon. We compare three cases with Λ CDM, namely the mode $k = 0.5 \text{ Mpc}^{-1}$ with $c_s^2 = 10^{-7}$, $k = 10 \text{ Mpc}^{-1}$ with $c_s^2 = 10^{-7}$ and $k = 0.5 \text{ Mpc}^{-1}$ with $c_s^2 = 1$. Only the first case corresponds to a mode outside the sound horizon, while the other two are well inside. Thus we see the same behaviour for $k = 10 \text{ Mpc}^{-1}$ with $c_s^2 = 10^{-7}$ and $k = 0.5 \text{ Mpc}^{-1}$ with $c_s^2 = 1$.

which we define for this purpose through $\Omega_m \Delta_m = \Omega_b \Delta_b + \Omega_{\text{cdm}} \Delta_{\text{cdm}}$. We compute Δ_m with the linear Boltzmann code CLASS and look at the evolution for wavenumbers $k = 0.5 \text{ Mpc}^{-1}$ and $k = 10 \text{ Mpc}^{-1}$ for the model with $c_s^2 = 10^{-7}$ which corresponds respectively to a mode well outside and a mode well inside the sound horizon. We compare the logarithmic growth rate from the two modes for $c_s^2 = 10^{-7}$, and in addition $k = 0.5 \text{ Mpc}^{-1}$ for $c_s^2 = 1$, with Λ CDM in the bottom right panel of Fig. 1. As expected, for the mode $k = 0.5 \text{ Mpc}^{-1}$ in the case where $c_s^2 = 1$, as it is well inside the sound horizon, the result matches with the mode evolution of $k = 10 \text{ Mpc}^{-1}$ in the case where $c_s^2 = 10^{-7}$. The mode $k = 0.5 \text{ Mpc}^{-1}$ has a different evolution in the case where $c_s^2 = 10^{-7}$ because it is outside the sound horizon and the perturbations in the dark energy field are therefore not suppressed.

3 OBSERVABLES

Solving the null geodesic equation ($k^\mu \nabla_\mu k_\nu = 0$) for a light ray with wavevector k^μ in a perturbed FLRW universe results in a change in position and energy of the light beam emitted from the source. The apparent comoving 3D position of the source reads (Bonvin & Durrer 2011; Challinor & Lewis 2011; Yoo et al. 2009; Breton et al. 2019; Adamek et al. 2020)

$$\mathbf{s} = \chi_s \mathbf{n} + \underbrace{\frac{1}{H_s(\bar{z})} \delta z \mathbf{n}}_{\text{redshift perturbation}} - \underbrace{\int_0^{\chi_s} (\chi_s - \chi) \nabla_\perp (\Phi + \Psi) d\chi}_{\text{weak gravitational lensing}} - \underbrace{\mathbf{n} \int_0^{\chi_s} (\Phi + \Psi) d\chi}_{\text{Shapiro time delay}}, \quad (10)$$

where \mathbf{s} is the observed position in redshift space, and \mathbf{n} and χ_s are respectively the unperturbed direction vector and

unperturbed comoving distance to the source. Furthermore, $\nabla_\perp \equiv (1 - \mathbf{n} \otimes \mathbf{n}) \nabla$ is the projected gradient perpendicular to the line of sight, χ is the comoving distance and $H_s(\bar{z})$ is the Hubble rate at the unperturbed redshift \bar{z} of the source. The first term in Eq. (10) corresponds to the unperturbed position, the second term corresponds to the redshift perturbation which is computed in Eq. (11), the third term (weak gravitational lensing) yields an angular deflection of the source position on the 2D sphere, and the last term changes the radial position due to the Shapiro time delay.

Using the time component of geodesic equation one obtains the redshift perturbation $\delta z = z - \bar{z}$ as

$$\delta z = (1 + \bar{z}) \left[\underbrace{\mathbf{n} \cdot (\mathbf{v}_s - \mathbf{v}_o)}_{\text{Doppler}} + \underbrace{\Psi_o - \Psi_s}_{\text{gravitational redshift}} - \underbrace{\int_0^{\chi_s} \frac{\partial(\Psi + \Phi)}{\partial \tau} d\chi}_{\text{ISW-RS effect}} \right]. \quad (11)$$

As a result of Eq. (10) and Eq. (11), the light ray along its path is deflected, redshifted and delayed due to the different physical phenomena, namely weak gravitational lensing, integrated Sachs-Wolfe and Rees-Sciama (ISW-RS) effect and Shapiro time delay. In addition, there are two local (non-integrated) contributions to the redshift: the relativistic Doppler effect (due to the peculiar velocities \mathbf{v}_s and \mathbf{v}_o of the source and observer, respectively) and the gravitational redshift (ordinary Sachs-Wolfe effect). Among these, the weak gravitation lensing, ISW-RS, Shapiro time delay and gravitational redshift all depend directly on the configuration of the gravitational field. If they can be observed independently they can be used as a probe of DE/MG. In the current work we are going to look at each individual aforementioned effect to study the impact of k -essence clustering dark energy. It is important to point out that the Doppler term is also expected to be a powerful probe of dark energy and is worth to be studied in detail. However, in this paper we only focus on the physical effects coming from the met-

ric perturbations Ψ and Φ . These have the advantage that they can be observed (as integrated effects) even in places where there are no visible sources, like e.g. in voids which are naturally expected to be dominated by dark energy.

In the following subsections we shall introduce and derive the relevant expressions for each effect separately and we will discuss why each of these observables could be potentially used to put constraint on DE/MG models, especially clustering dark energy.

3.1 Weak gravitational lensing

The light from distant objects is deflected due to inhomogeneities as it travels through the intervening large scale structure in the Universe. The deflection angles are usually small at cosmological scales and this phenomenon is called weak gravitational lensing. As mentioned already, weak gravitational lensing directly probes the distribution of matter and energy, including dark matter and dark energy, which makes it a unique tool to constrain the cosmological parameters (Bartelmann & Schneider 2001; Hikage et al. 2019; Ade et al. 2014a; Lewis & Challinor 2006; Hassani et al. 2016; Refregier 2003). Weak gravitational lensing can be observed through the statistics of cosmic shear and cosmic convergence, as we will summarise briefly in the following.

Cosmic shear refers to the change of the ellipticities of galaxies observed on the far side of the gravitational lens. The cosmic convergence, on the other hand, magnifies/demagnifies the sizes and magnitudes of the same galaxies (Alsing et al. 2015; Mandelbaum 2018). The first detection of cosmic shear have been done about 20 years ago (van Waerbeke et al. 2000; Bacon et al. 2000), while cosmic convergence was measured for the first time in 2011 (Schmidt et al. 2012). Since then the precision in cosmic shear and cosmic convergence measurements has been improved and these two have become some of the most promising probes of dark energy and modified gravity (Jain & Taylor 2003; Spurio Mancini et al. 2018; Hannestad et al. 2006; Amendola et al. 2008).

In Adamek et al. (2019), some of us have implemented a ray-tracing method to analyse relativistic N -body simulations performed with the code *gevolution*. In this method one solves the optical equations in the scalar sector of gravity without any approximation and additionally keeps track of the frame dragging to first order. Weak-lensing convergence and shear obtained with this numerical method were studied in more detail in Lepori et al. (2020). While other approaches often try to reconstruct the signal from the mass distribution, our method works with the metric perturbations directly and is therefore more robust once we consider DE/MG like in the present work. To this end we have recently implemented the same light-cone analysis and ray-tracing method in k -evolution. Here, however, we compute each effect only to first order in Φ and Ψ , and we neglect the frame dragging. For the purpose of discussing angular power spectra this is sufficient, as nonperturbative effects (in the

ray tracing²) would only enter at a detectable level for very high multipoles that are not resolved in our maps.

In the first order weak gravitational lensing formalism one introduces the lensing potential $\psi(\mathbf{n}, z)$ defined as

$$\psi(\mathbf{n}, z) \equiv - \int_0^{\chi_s} d\chi \frac{\chi_s - \chi}{\chi_s \chi} (\Phi + \Psi), \quad (12)$$

where the redshift z and the source distance χ_s are related through the background distance-redshift relation, and the integration is carried out in direction \mathbf{n} using the Born approximation.

Using the gradient $\hat{\nabla}^a$ on the 2D sphere we can calculate the deflection angle as $\alpha^a = \theta_o^a - \theta_s^a = \hat{\nabla}^a \psi$, which results in the lensing term in Eq. (10). The Jacobi map, which is a map between the unperturbed source angular positions θ_s and the observed angular positions θ_o , i.e. $\mathcal{A}_{ab} = \partial \theta_o^a / \partial \theta_s^b$, contains the full information for weak gravitational lensing and reads

$$\mathcal{A} = \begin{pmatrix} 1 - \kappa - \gamma_1 & \omega - \gamma_2 \\ -\omega - \gamma_2 & 1 - \kappa + \gamma_1 \end{pmatrix}, \quad (13)$$

which at leading order is rewritten in terms of the gradients of the lensing potential,

$$\mathcal{A} = \mathbb{1} + \left(\hat{\nabla}_a \hat{\nabla}_b \psi \right). \quad (14)$$

Note that this also implies $\omega = 0$ at leading order. We can extract the convergence κ and the complex shear from the lensing potential as

$$\kappa = -\frac{1}{2} \hat{\nabla}^2 \psi, \quad (15)$$

$$\gamma \equiv \gamma_1 + i\gamma_2 = -\frac{1}{2} \left(\hat{\nabla}_1^2 - \hat{\nabla}_2^2 \right) \psi - i\hat{\nabla}_1 \hat{\nabla}_2 \psi \quad (16)$$

The relation between a non-perturbative geometrical description and these first-order quantities is discussed in detail in Lepori et al. (2020).

The lensing potential, convergence and complex shear as scalar functions on the 2D sphere may be expanded in the basis of spherical harmonics $Y_{\ell m}(\mathbf{n})$,

$$X(\mathbf{n}) = \sum_{\ell m} X_{\ell m} Y_{\ell m}(\mathbf{n}). \quad (17)$$

Assuming that these functions obey statistical isotropy, the two-point function of the expansion coefficients $X_{\ell m}$ is diagonal in ℓ and m and we can define the angular power spectrum C_ℓ as,

$$\langle X_{\ell m} X_{\ell' m'} \rangle \equiv \delta_{\ell \ell'} \delta_{m m'} C_\ell^X. \quad (18)$$

Our code uses directly Eq. (12) to construct the lensing map and then computes the angular power spectrum from the map. We can however also compute an expression for the weak-lensing C_ℓ^κ by considering the two-point function of the integrand of Eq. (12) and using Eq. (15) in harmonic space,

$$C_\ell^\kappa = 4\pi^2 \ell^2 (\ell + 1)^2 \int_0^\infty k^2 dk \int_0^{\chi_s} d\chi \frac{\chi_s - \chi}{\chi_s \chi} \int_0^{\chi_s} d\chi' \frac{\chi_s - \chi'}{\chi_s \chi'} \times [1 + \eta(k, \chi)] [1 + \eta(k, \chi')] j_\ell(k\chi) j_\ell(k\chi') P_\Phi(k, \chi, \chi'), \quad (19)$$

² We remind the reader that Φ and Ψ themselves represent non-perturbative solutions obtained with full simulations.

where $P_\Phi(k, \chi, \chi')$ is the unequal-time correlator of the gravitational potential in Fourier space defined by

$$\langle \Phi(\mathbf{k}, \chi) \Phi^*(\mathbf{k}', \chi') \rangle = (2\pi)^3 \delta_D(\mathbf{k} - \mathbf{k}') P_\Phi(k, \chi, \chi'). \quad (20)$$

Moreover, according to Eq. (8) the gravitational potential unequal-time correlator may be written based on the one of matter as follows,

$$P_\Phi(k, \chi, \chi') = k^{-4} (4\pi G_N \bar{\rho}_m^0)^2 \mu(k, \chi) \mu(k, \chi') \times [1 + \bar{z}(\chi)] [1 + \bar{z}(\chi')] P_{\Delta_m}(k, \chi, \chi'). \quad (21)$$

In the last few equations, we use the shorthand $\mu(k, \chi)$ for $\mu(k, z(\chi))$ and similar for η , P_Φ and so on.

The lensing signal, as a result, responds to the DE/MG models in multiple ways: at the background level through a change in the distance-redshift relation, and at the level of perturbations through a modified growth and through the modifications encoded in the $\mu(k, z)$ and $\eta(k, z)$ parameters (Spurio Mancini et al. 2018; Takahashi et al. 2017), specifically through the combination $\Sigma = \mu(1 + \eta)/2$ that describes the modification of the lensing potential (Amen-dola et al. 2008). In Sec. 5 we will compute the lensing signal for two fixed source redshifts, namely $z = 0.85$ and $z = 3.3$, in N -body simulations to study the effects of dark energy clustering and of the expansion history on the lensing.

It is also worth mentioning that at leading order in the absence of systematics and shape noise (K  hlinger et al. 2017) the convergence angular power spectrum contains the full lensing information. Decomposing the shear into rotationally-invariant E and B components one can show from Eq. (14) that (Becker 2013)

$$C_\ell^{\gamma^E} = \frac{1}{\ell^2(\ell+1)^2} \frac{(\ell+2)!}{(\ell-2)!} C_\ell^\kappa, \quad (22)$$

$$C_\ell^{\gamma^B} = \frac{1}{\ell^2(\ell+1)^2} \frac{(\ell+2)!}{(\ell-2)!} C_\ell^\omega = 0.$$

In the following sections we therefore only discuss the convergence power spectra.

3.2 Integrated Sachs-Wolfe and non-linear Rees-Sciama effect

If the light rays from source galaxies traverse a time-dependent gravitational potential then in general their energy will change (Sachs & Wolfe 1967). Specifically, the light is redshifted for rays passing through a growing potential well, and blueshifted if the potential well is decaying. This effect is known as late integrated Sachs-Wolfe effect (late ISW) and is a powerful probe of dark energy at low multi-poles.

During matter domination and in linear perturbation theory the gravitational potential wells remain constant in time and as a result the photons do not gain or lose energy along their trajectories after accounting for the expansion of the background. But when dark energy becomes important and the expansion rate of the Universe deviates from the matter-dominated behaviour, the gravitational potential decays at linear scales. As a result, photons gain energy and are blueshifted as they travel through over-dense regions while they lose energy and are redshifted as they travel through voids (Carbone et al. 2016; Ade et al. 2016b). In this way, the late ISW effect induces additional anisotropies in the power

spectrum of the cosmic microwave background (CMB) radiation, primarily at large scales. These anisotropies are correlated with the large-scale structure as they are due to evolving gravitational potential wells.

In addition to this effect in linear perturbation theory, the perturbations on small scales and at late times evolve non-linearly. The non-linear large scale structure of the Universe induces additional energy changes in the light rays as they pass through these structures. This so-called Rees-Sciama effect (Rees & Sciama 1968) enhances the ISW effect in under-dense regions and decreases it in the over-dense regions as the non-linear growth of structure acts opposed to dark energy (Cai et al. 2010).

The linear late ISW and non-linear Rees-Sciama effects (abbreviated as ISW-RS when combined) are sensitive to the background evolution and growth of structures at late times, when the dark energy dominates over other components (Cabass et al. 2015; Adamek et al. 2020; Beck et al. 2018; Khosravi et al. 2016).

Direct measurements of the ISW-RS signal from CMB data is demanding, and as a result it is detected indirectly, either by cross-correlating large scale structure data and CMB maps (Scranton et al. 2003; Seljak 1996; Francis & Peacock 2010; Peiris & Spergel 2000; Ade et al. 2016c) or by stacking clusters and voids to enhance the signal (Granett et al. 2008; Ade et al. 2016c; Cai et al. 2017, 2014). The effect is also detected through the ISW-lensing bispectrum using Planck data (Ade et al. 2014b).

According to Eq. (11), the term responsible for the ISW-RS effect yields a change in CMB temperature,

$$\Theta(\mathbf{n}, z) \equiv \frac{\Delta T}{T} = -\frac{\delta z}{1 + \bar{z}} = \int_0^{\chi_s} \frac{\partial(\Psi + \Phi)}{\partial \tau} d\chi, \quad (23)$$

where χ_s is the distance to the last-scattering surface for the CMB. In the presence of DE/MG the gravitational potentials Φ and Ψ are modified as a result of Eq. (8) and Eq. (9) for the gravitational slip and clustering parameters $\eta(k, z)$, $\mu(k, z)$. It is also interesting to note that these modifications are projected in a different way for the ISW-RS signal and the lensing signal, and thus these two could probe DE/MG in independent ways. Following the discussion in the previous subsection, $\Theta(\mathbf{n}, z)$ may be expanded in terms of spherical harmonics and one can compute the ISW-RS angular power spectrum. Taking the time derivative of the Hamiltonian constraint (the modified Poisson equation) (8), and replacing Ψ through (9), results in a constraint equation for $\partial(\Phi + \Psi)/\partial \tau$ which in general is a function of $\mu(k, z)$, $\eta(k, z)$ and their time derivatives:

$$\frac{\partial(\Phi + \Psi)}{\partial \tau} = 4\pi G_N a^2 \bar{\rho}_m \Delta_m \frac{H(z)}{k^2} \left[\mu(k, z) \frac{\partial \eta(k, z)}{\partial z} - (1 + \eta(k, z)) \left(\mu(k, z) \frac{f(k, z) - 1}{1 + z} - \frac{\partial \mu(k, z)}{\partial z} \right) \right] \quad (24)$$

Writing this as $\partial(\Phi + \Psi)/\partial \tau = g(k, z) \Delta_m$ we find

$$C_\ell^\Theta = 16\pi^2 \int_0^\infty k^2 dk \int_0^{\chi_s} d\chi \int_0^{\chi_s} d\chi' j_\ell(k\chi) j_\ell(k\chi') \times g(k, \chi) g(k, \chi') P_{\Delta_m}(k, \chi, \chi'). \quad (25)$$

In this article we use ray tracing to compute the ISW-RS signal according to Eq. (23) by integrating along the past

light cone to the source redshifts $z = 0.85$ and $z = 3.3$ as in the previous section. This can be seen either as a direct contribution to the observed redshift of the sources, or as a fractional contribution to the CMB temperature anisotropy that captures the part of the signal that is generated by the structure out to that distance and that could therefore be constrained through a cross-correlation of the CMB with large-scale structure. We use the ISW-RS angular power spectra in Sec. 5 to measure the response of this signal to different k -essence scalar field scenarios.

3.3 Gravitational redshift

The light rays emitted from source galaxies in the potential well of galaxy clusters and dark matter halos are expected to be redshifted/blueshifted due to the difference in gravitational potential between the source galaxy and the observer. This effect is known as gravitational redshift (Cappi 1995), or as ordinary Sachs-Wolfe effect in the context of CMB physics (Durrer 2001), and is the second term in the full expression written in Eq. (11),

$$\delta z_{\text{grav}} = (1 + \bar{z}) (\Psi_o - \Psi_s). \quad (26)$$

For typical cluster masses (of order $\sim 10^{14} M_\odot$) the gravitational redshift is estimated to be two orders of magnitude smaller than the Doppler shift [the first term in Eq. (11)] coming from the random motion of source galaxies (Cappi 1995). The technique to extract the gravitational redshift signal from other dominant signals depends on the fact that the Doppler shift results in a symmetric dispersion in the redshift-space distribution, while the gravitational redshift changes the mean of the distribution (Broadhurst & Scannapieco 2000; Kim & Croft 2004). In Wojtak et al. (2011) the first measurement of gravitational redshift of light coming from galaxies in clusters was carried out by stacking 7800 clusters from the SDSS survey in redshift space. The signal detection was used to rule out models avoiding the presence of dark matter and also to show the consistency of the results with the predictions of general relativity. The gravitational redshift signal was detected [e.g. in Sadeh et al. (2015); Jimeno et al. (2015)] on scales of a few Mpc around galaxy clusters and recently in elliptical galaxies (Zhu et al. 2019) using spectra from the Mapping Nearby Galaxies at Apache Point Observatory (MaNGA) experiment.

The gravitational redshift as an observable is a prominent and direct probe of gravity at cosmological scales (Wojtak et al. 2011; Alam et al. 2017). We expect to see the effect of dark energy perturbations directly in the gravitational redshift signal since $\Psi \propto \mu(k, z)\eta(k, z)\Delta_m$, see Eqs. (8) and (9). Hence,

$$C_\ell^{\delta z_{\text{grav}}} = 36\pi^2 H_0^4 \Omega_m^2 [1 + \bar{z}(\chi_s)]^4 \times \int_0^\infty \frac{dk}{k^2} j_\ell^2(k\chi_s) \mu^2(k, \chi_s) \eta^2(k, \chi_s) P_{\Delta_m}(k, \chi_s). \quad (27)$$

In Sec. 5 we study the effect of k -essence dark energy on the gravitational redshift signal.

3.4 Shapiro time delay

In addition to all the effects discussed in the previous sections, the gravitational potential of large-scale structure per-

turbs the interval of cosmic time while a photon traverses a given coordinate distance. This effect is known as Shapiro time delay and is first discussed and introduced in Shapiro (1964) as a fourth test of general relativity.

While the gravitational lensing is due to the gradient of the projected potentials along the photon trajectories and is weighted by the lensing kernel, the Shapiro time delay is proportional to the projected potential itself. As a result we expect much more signal at high multipoles from the lensing convergence compared to the Shapiro time delay, due to the additional factor of $\sim \ell^2$.

Due to Shapiro time delay the last scattering surface is a deformed sphere as different light rays travel through different gravitational potentials to reach us. All the photons we receive from the last scattering surface were released almost at the same time, so the time delay means that the photons reaching us from different directions have started at different distances from us. The modulation of the spherical surface due to Shapiro time delay is ~ 1 Mpc (Hu & Cooray 2001). The effect of Shapiro time delay on the CMB temperature and polarisation anisotropies is studied in Hu & Cooray (2001). They show that, while it is difficult to extract the Shapiro time delay signal from the data, neglecting it would introduce a systematic error. They argue that the Shapiro time delay should be considered in order to reduce the systematics in the analysis, especially for future high precision experiments.

In Li et al. (2019) an estimator quadratic in the temperature and polarization fields is introduced to provide a map of the Shapiro time delays as a function of position on the sky. They show that the signal to noise ratio of this map could exceed unity for the dipole, so the signal could be used to provide an understanding of the Universe on the largest observable scales.

As discussed in Nusser (2016), for tests of the equivalence principle at high redshift that rely on the Shapiro time delay effect, potential fluctuations from the large scale structure of the Universe are at least two orders of magnitude larger than the gravitational potential of the Milky Way. This suggests that the effect of dark energy on these potentials needs to be considered in order to model the Shapiro time delay accurately. From the last term in Eq. (10) we get

$$\Delta\tau = (1 + \bar{z}) \Delta t = - \int_0^{\chi_s} (\Phi + \Psi) d\chi, \quad (28)$$

and hence

$$C_\ell^{\Delta\tau} = 16\pi^2 \int_0^\infty k^2 dk \int_0^{\chi_s} d\chi \int_0^{\chi_s} d\chi' j_\ell(k\chi) j_\ell(k\chi') \times [1 + \eta(k, \chi)] [1 + \eta(k, \chi')] P_\Phi(k, \chi, \chi'). \quad (29)$$

The dependence on $\mu(k, z)$ is evident from Eq. (21). This expression can be compared to Eq. (19) where dark energy enters identically in the integrand, but the effect is weighted differently along the line of sight due to the lensing kernels. In our numerical analysis we obtain sky maps of the Shapiro time delay by directly solving Eq. (28).

4 SIMULATIONS

The results presented in this paper are based on simulations performed with the relativistic N -body codes k -

evolution (Hassani et al. 2019), which includes non-linearly clustering dark energy in the form of a k -essence scalar field, and *gevolution* (Adamek et al. 2016a) for Λ CDM and cases where linear dark energy perturbations are sufficient [see Fig. 1 in Hassani et al. (2019)]. We also compare our results from these two N -body codes with the linear Boltzmann code CLASS (Blas et al. 2011).

In *gevolution* and k -evolution, for a fixed observer, a “thick” approximate past light cone is constructed that encompasses a region sufficiently large to permit the reconstruction of the true light cone following the deformed photon trajectories in post-processing (Adamek et al. 2019). The metric information for this thick light cone is saved in spherical coordinates pixelised using HEALPix (Gorski et al. 2005). This lets us compute light-cone observables including weak gravitational lensing, ISW-RS, Shapiro time delay and gravitational redshift in post-processing. In the present work we use a fast pixel-based method to solve the integrals of Eqs. (12), (23) and (28) in the Born approximation, given that post-Born corrections typically affect the angular power spectra only at very high multipoles. A comparison of this approach with “exact” ray tracing of the deformed geodesics is presented in Lepori et al. (2020) for the case of the weak lensing convergence [see also Pratten & Lewis (2016)] and justifies the use of the Born approximation for the multipoles discussed here. Note, however, that post-Born corrections can play an important role in higher-order correlation functions like the angular bispectrum.

For illustration, in Fig. 2 the maps of each physical effect from a Λ CDM simulation are shown in the left panels. In the right panels the difference between the maps from k -essence with $w_0 = -0.9$ and $c_s^2 = 10^{-7}$ and k -essence with $w_0 = -0.9$ and $c_s^2 = 1$ are shown. Since the seed number of the simulations are identical, this shows the effect of k -essence clustering on each map, because k -essence does not cluster significantly for the case with high speed of sound squared, $c_s^2 = 1$.

In our simulations we place the observer in the corner of the box at position (0,0,0) in Cartesian coordinates. We store data on the past light cone of the observer on the full sky out to a comoving distance of $\chi_s = 2015 \text{ Mpc}/h$, which corresponds approximately to $z = 0.8$, and out to a comoving distance of $\chi_s = 4690 \text{ Mpc}/h$ or a corresponding approximate redshift of $z = 3.3$ for a pencil beam covering a sky area of 1932 sq. deg. in the direction of the diagonal of the simulation box.

The simulation boxes have a comoving size of $L = 4032 \text{ Mpc}/h$. The fields evolve on a grid with $N_{\text{grid}} = 4608^3$ grid points, and the matter phase space is sampled by $N_{\text{pcl}} = 4608^3$ (i.e. about 100 billion) particles. We use the following cosmological parameters for all runs: the amplitude of scalar perturbations is set to $A_s = 2.1 \times 10^{-9}$ at the pivot scale $k_p = 0.05 \text{ Mpc}^{-1}$, the scalar spectral index is $n_s = 0.96$, the Hubble parameter $h = 0.67$, cold dark matter and baryon densities are, respectively, $\omega_{\text{cdm}} = \Omega_{\text{cdm}} h^2 = 0.121203$ and $\omega_b = \Omega_b h^2 = 0.021996$, and the CMB temperature $T_{\text{CMB}} = 2.7255 \text{ K}$. We also include two massive neutrino species with masses $m_1 = 0.00868907 \text{ eV}$ and $m_2 = 0.05 \text{ eV}$ with temperature parameter $T_{\text{C}\nu\text{B}} = 1.95176 \text{ K}$, as well as $N_{\text{ur}} = 1.0196$ massless neutrinos (Adamek et al. 2017a). The effect of neutrino and radiation perturbations is approximated using the linear transfer functions from CLASS as

described in Brandbyge & Hannestad (2009) and Adamek et al. (2017b), respectively. We only consider spatially flat universes, $\Omega_k = 0$, so that the dark energy density parameter is given by $\Omega_{\text{DE}} = 1 - \sum_X \Omega_X$ where the sum goes over all species except dark energy. For the simulations where the dark energy is not a cosmological constant, we use a constant equation of state relation given by $w_0 = -0.9$ and $w_a = 0$.

The initial conditions for the simulations are set using the linear transfer functions from CLASS at $z = 100$ and all the simulations are run with the same seed number which helps us to compare the results.

For our k -essence cosmology we consider three different choices for the speed of sound: $c_s^2 = 1$, $c_s^2 = 10^{-4}$ and $c_s^2 = 10^{-7}$. Strong non-linear clustering of the dark energy field is only expected in the last case, and to study this specific aspect, we run two separate simulations for this case. In one simulation we use the code *gevolution* which approximates the dark energy perturbations by their solution from linear theory, see Hassani et al. (2019) for more details. In the other simulation we use the code k -evolution in order to keep track of the dark energy field’s response to the non-linear clustering of matter. For the higher values of the speed of sound we only run k -evolution. We also do a reference run for the Λ CDM model with *gevolution* – here there is no difference between the two codes because dark energy perturbations are absent.

5 NUMERICAL RESULTS

In this section we show the results of our numerical simulations. Once we have generated the maps with our pixel-based numerical integrator we use ANAFast from the PYTHON package of HEALPix to compute the angular power spectra and cross power spectra. However, for the pencil beam maps that cover only about 5% of the sky we instead use the pseudo- C_ℓ estimator of Wandelt et al. (2001); Szapudi et al. (2000) to obtain the power spectra in an unbiased way. To do so we use the POLSPICE package to compute the angular power spectra and cross power spectra of the masked maps.

5.1 Weak gravitational lensing

In the top panel of Fig. 3 the angular power spectra for the lensing convergence from k -evolution, *gevolution* and CLASS integrating up to $\chi_s = 2000 \text{ Mpc}/h$ are shown, which corresponds to a source redshift of approximately $z = 0.85$. On the top the data points show the results for $\ell(\ell+1)C_\ell^\kappa$ of two simulations with $c_s^2 = 10^{-7}$ and $c_s^2 = 1$, as well as for Λ CDM. In addition, results for CLASS are shown for the case $c_s^2 = 10^{-7}$ as dash-dotted and dotted lines, respectively using linear theory alone or Halofit (Takahashi et al. 2012) to model the non-linear matter power spectrum.

The effect of matter non-linearities appears in the convergence power spectrum at $\ell \sim 100$ where both Halofit and N -body simulation data start to diverge from the linear prediction. In the bottom panel of Fig. 3 the relative difference between the convergence power spectra of different models are shown (we always keep χ_s fixed which means that the source redshift can vary by a small amount depending on the background cosmology). This quantifies the effect of dark energy at different levels and can be

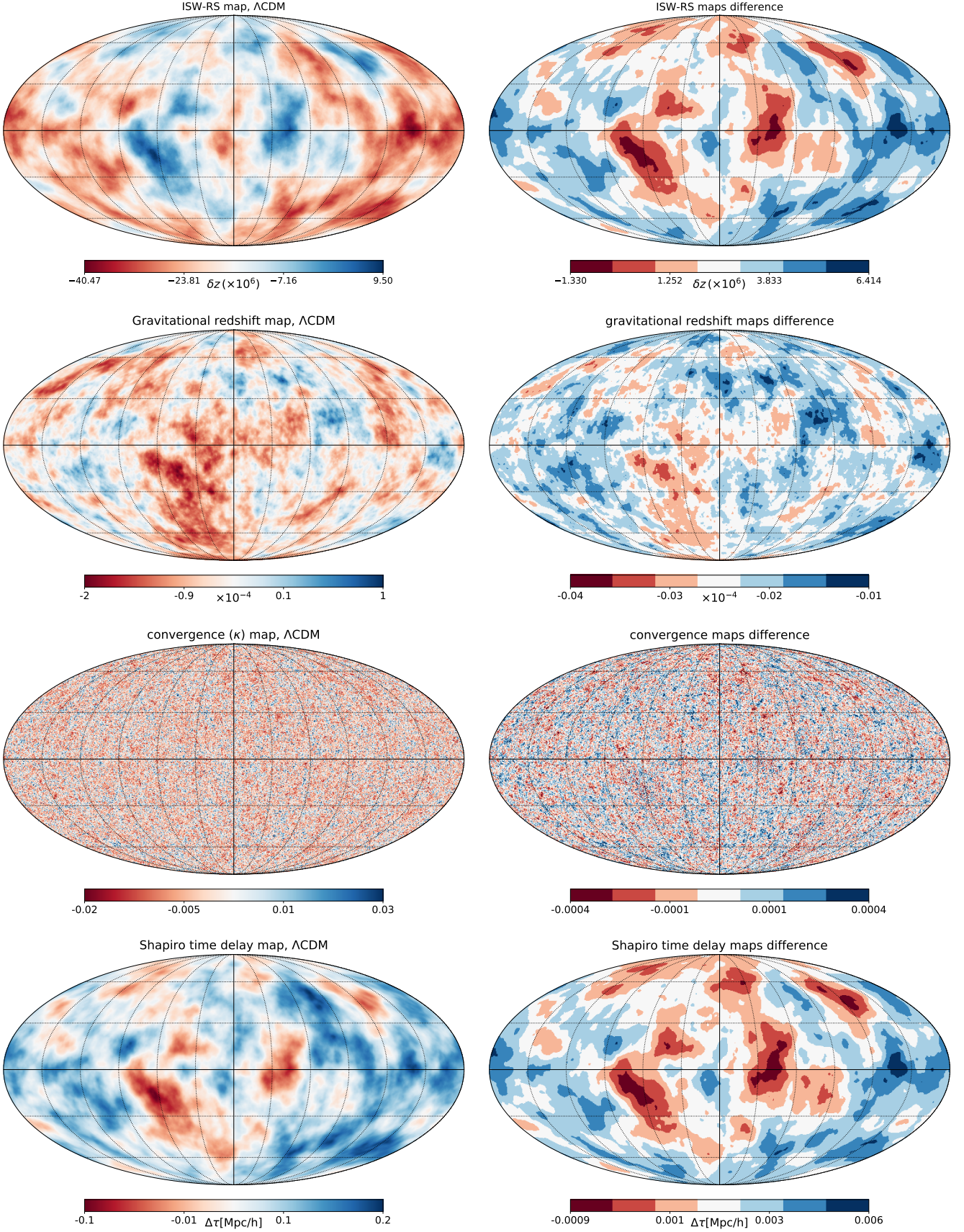


Figure 2. *Left:* Full-sky maps of the ISW-RS temperature anisotropy, gravitational redshift, convergence and Shapiro time delay from a Λ CDM simulation using *gevolution*, integrated to $z \sim 0.8$ are shown. *Right:* Difference between the maps for k -essence with $c_s^2 = 10^{-7}$ and k -essence with $c_s^2 = 1$, both simulated with *k*-evolution. All simulations used the same seed to generate the random initial conditions and hence the difference maps indicate the importance of k -essence clustering.

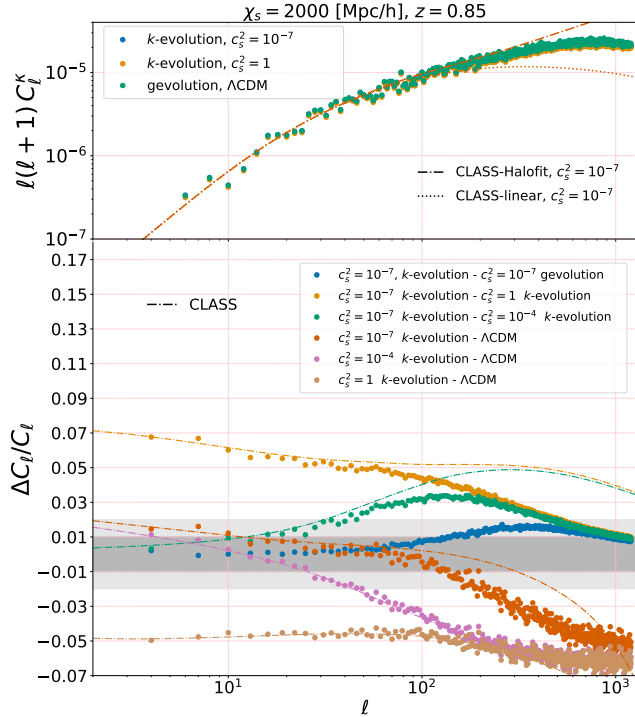


Figure 3. *Top panel:* The angular power spectra of the lensing convergence κ at a source distance of $\chi_s = 2000$ Mpc/h for some of our N -body simulations, as well as predictions from CLASS with and without the Halofit prescription. Based on the convergence test of App. A we can trust the convergence spectrum here to $\ell \approx 200$, which is roughly where the dots start to deviate from the CLASS-Halofit curve. Relative spectra remain accurate to much higher ℓ . *Bottom panel:* Data points show the relative difference between the convergence power spectra from our N -body simulations for different models, whereas dashed lines represent the corresponding predictions from CLASS with Halofit, shown in matching colours. The blue points show the impact of k -essence non-linearities by comparing non-linear k -essence from k -evolution with its linear implementation in *gevolution*.

compared to the prediction from CLASS. The data points show again the numerical results from our N -body simulations, whereas the CLASS/Halofit results for the same model comparisons are plotted as dashed lines using the same colours. Note that the comparison between k -evolution and *gevolution* for the case $c_s^2 = 10^{-7}$ has no corresponding prediction from CLASS, and quantifies the importance of the nonlinear modelling of k -essence within the N -body simulations. To be specific, our convention is $\Delta C_\ell/C_\ell = (C_\ell^{(\text{dataset 1})} - C_\ell^{(\text{dataset 2})})/C_\ell^{(\text{dataset 2})}$, where “dataset 1” and “dataset 2” are indicated in the legend of each figure.

At large scales, as expected, the results from CLASS and N -body simulations agree very well, while at smaller scales some deviations are seen. The deviation of the N -body results from the CLASS/Halofit prediction occurs mainly when there is dark energy clustering which is more pronounced for the cases with low speed of sound. Indeed, comparing the case $c_s^2 = 1$ with Λ CDM we find that the CLASS/Halofit prediction is accurate at least up to $\ell \sim 1000$, whereas for the lowest speed of sound, $c_s^2 = 10^{-7}$, significant disagreement between CLASS/Halofit and N -body

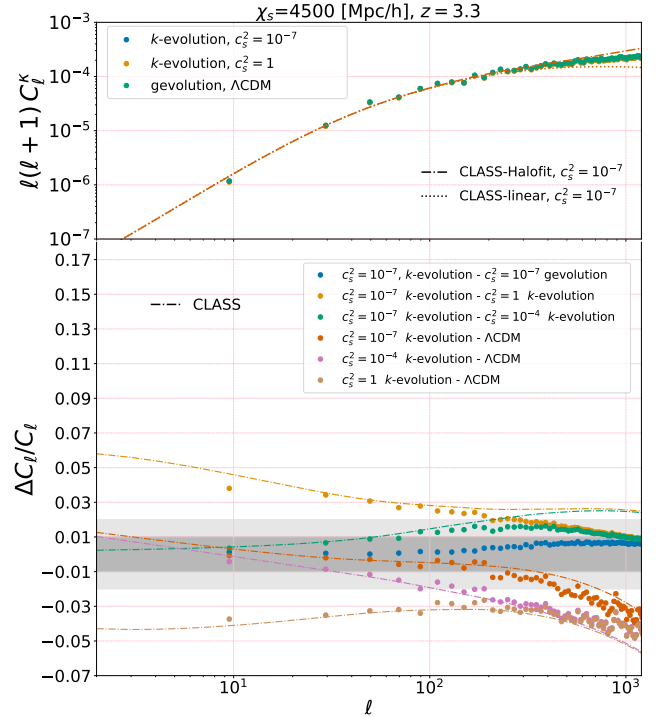


Figure 4. Same as Fig. 3, but for a source distance of $\chi_s = 4500$ Mpc/h, corresponding roughly to $z \approx 3.3$, and using N -body simulation data that covers $\sim 5\%$ of the sky. Again based on App. A we can trust the dots in the top panel to $\ell \approx 500$, while the relative spectra shown in the bottom panel are again valid to higher ℓ .

simulations appears already for multipoles $\ell \gtrsim 100$. This is in complete agreement with our results in Hassani et al. (2020) where we show that CLASS/Halofit gives the right clustering function $\mu(k, z)$ for high speed of sound.

Our comparison between the two simulation methods (k -evolution and *gevolution*) for the case $c_s^2 = 10^{-7}$ shows that the non-linear response of k -essence to matter clustering produces an effect of $\sim 2\%$ in the convergence power spectrum at multipoles in the range of a few hundred.

According to Fig. 3 the effect of dark energy clustering can cancel the effect of the background evolution with $w_0 = -0.9$ on the weak-lensing signal at large angular scales: the $\sim 5\%$ suppression when going from Λ CDM to w CDM with $c_s^2 = 1$ is compensated by an amplification of similar size when going from $c_s^2 = 1$ to low speed of sound. The scale up to which this cancellation works is set by the sound horizon, and at very non-linear scales there is always some residual suppression.

Fig. 4 is similar to Fig. 3 but shows results from the pencil beam map integrating to a higher source distance of $\chi_s = 4500$ Mpc/h, corresponding approximately to redshift $z = 3.3$. As we have access to only $\sim 5\%$ of the sky in this case, we have no information about the angular power spectra at low ℓ . The CLASS/Halofit and N -body simulation data agree better compared to the lower redshift results, as the scale where the finite resolution of the simulation affects the result is shifted to higher multipoles, see Appendix A [cf. also Appendix C of Lepori et al. (2020)]. Moreover, the

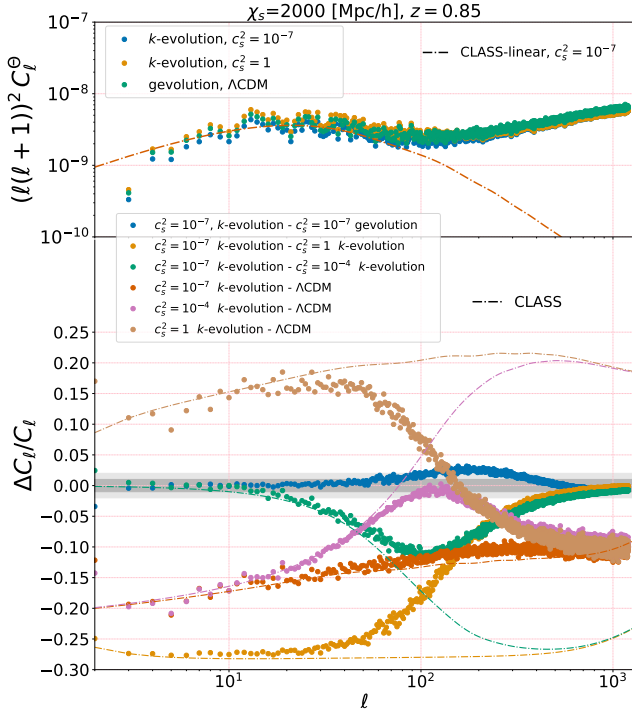


Figure 5. Top panel: The late-ISW-RS angular power spectra for different cosmologies integrating to $\chi_s = 2000$ Mpc/h are shown. Note that CLASS only predicts the linear ISW signal without any non-linear correction applied. The convergence study of App. A indicates that these spectra are reliable to $\ell \approx 500$, the relative spectra are again valid to higher ℓ . **Bottom panel:** The relative difference between different models in the ISW-RS power spectra are shown. At large scales the result from N -body codes agree with CLASS, however, already at $\ell < 100$ the linear and non-linear curves diverge due to the non-linear RS effect.

relative difference between the angular power spectra is less substantial compared to lower redshift result which comes from the fact that dark energy starts to dominate at lower redshift and integrating to higher redshifts therefore effectively dilutes the signal.

The overall signal amplitude for lensing is larger at higher redshift owing to the fact that it is an integrated effect. Thus, although the relative effect of dark energy clustering is lower at higher redshifts, the detectability of the signal is larger, and combining high and low redshift lensing data still significantly increases the signal to noise ratio.

5.2 ISW-RS effect

In Figs. 5 and 6, the ISW-RS angular power spectra from our N -body simulations and CLASS are shown and the different dark energy models are compared in the bottom panel of each figure. The ISW-RS signal is very sensitive to the clustering of dark energy and also its background evolution. Comparing dark energy with low and high speeds of sound with Λ CDM, one finds a huge impact $\sim 35\%$ at $z = 3.3$ and $\sim 30\%$ at $z = 0.85$ from dark energy clustering which makes the ISW-RS signal an excellent probe of this model.

It is also interesting to see that the non-linear RS effect starts to have impact at larger scales than the scale of non-

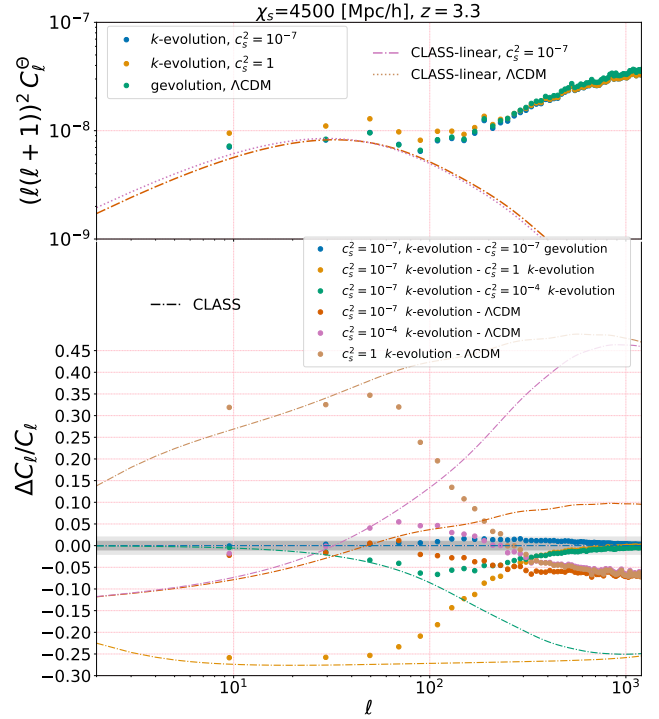


Figure 6. Same as Fig. 5, but for a source distance of $\chi_s = 4500$ Mpc/h, corresponding roughly to $z \approx 3.3$, and using N -body simulation data that covers $\sim 5\%$ of the sky. From the convergence study in the appendix we conclude that these spectra are reliable over the full range of scales shown.

linearity in the lensing signal in Fig. 4 which is also observed and discussed in (Cai et al. 2009; Adamek et al. 2020). To verify that the non-linear RS indeed appears in lower moments we design a numerical experiment to decrease the non-linear RS signal by decreasing A_s , the amplitude of scalar perturbations. This shifts the non-linear scale and allows us to separate the linear ISW effect from higher-order corrections. Our numerical results, shown in Appendix B, verify that the non-linear RS effect is responsible for the deviation at lower ℓ compared to lensing. This is maybe not too surprising given that the lensing kernel suppresses contributions from the vicinity of the observer which would be projected dominantly to low multipoles.

The non-linear RS effect is not implemented in CLASS and as a result we see power drop at $\ell \sim 100$ in the linear power spectra (top panels). Moreover, it is interesting to see that unlike the lensing power spectra, the effect of clustering dark energy and background evolution do not cancel each other in the ISW-RS power spectra and we obtain $\sim -20\%$ relative difference between $c_s^2 = 10^{-7}$ and Λ CDM.

As seen in Fig. 6 the signal itself is stronger at higher redshift as it is an integrated signal. However, depending on the parameters the relative difference can change positively or negatively compared to the lower redshift comparison. This is because more linear ISW and less non-linear effect is accumulated at high redshift.

As explained in Sec. 3.2 the direct detection of ISW-RS signal is difficult and it is therefore usually detected indirectly, e.g. via cross correlation with other quantities.

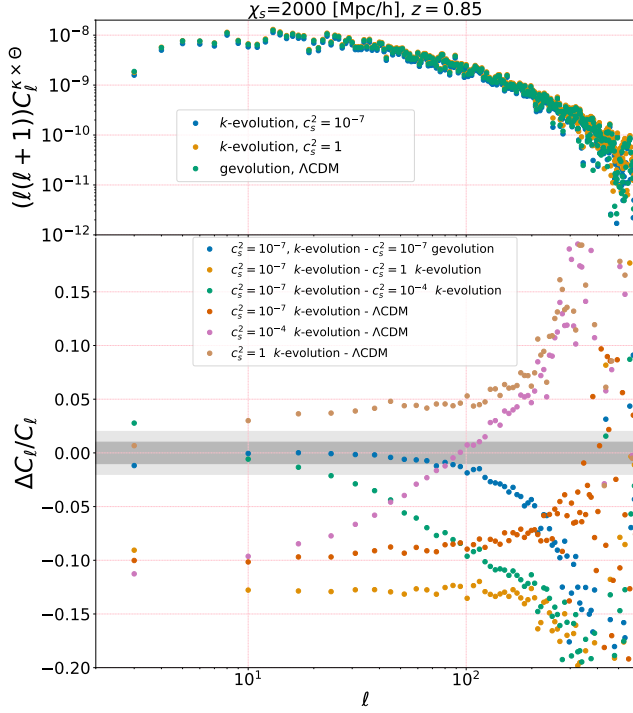


Figure 7. *Top panel:* The cross power spectra of lensing convergence κ and ISW-RS integrated to comoving distance $\chi_s = 2000$ Mpc/h from k -evolution with two speeds of sound $c_s^2 = 10^{-7}$ and $c_s^2 = 1$ are shown, together with our Λ CDM reference run. *Bottom panel:* The relative difference between the cross power spectra for several models is shown.

As an example, we report the convergence-ISW-RS cross power spectra in Fig. 7 and Fig. 8. Fig. 9 shows the cross-correlation coefficient, i.e. the cross power normalised to the r.m.s. of each individual signal. The effects of dark energy clustering and expansion history in the cross power spectra follows similar trends as seen for the individual probes. Interestingly, the cross-correlation coefficient saturates to ~ 0.8 at low ℓ almost independently of the dark energy model. This is because virtually all the effect is taken up by the normalisation. However, the non-linear evolution is different in different models, which leads to an absolute change, ΔC_{ℓ} , in the cross-correlation coefficient of a few percentage points at high multipoles.

5.3 Gravitational redshift

In Fig. 10 the gravitational redshift angular power spectra for different scenarios are compared. The top panel shows $\ell(\ell+1)C_{\ell}^{\delta_{\text{grav}}}$ for three cases, and the bottom panel the relative difference between different angular power spectra. Like for the lensing signal, the effect of clustering and background almost cancel at large scales by coincidence: Comparing power spectra from dark energy with two different speeds of sound ($c_s^2 = 1$ and $c_s^2 = 10^{-7}$) we find a difference of $\sim 2\%$ due to the clustering of dark energy. The relative difference between Λ CDM with w CDM with $c_s^2 = 1$ reaches $\sim -3\%$ due to different background evolution. But the difference between Λ CDM and k -essence with a low sound speed

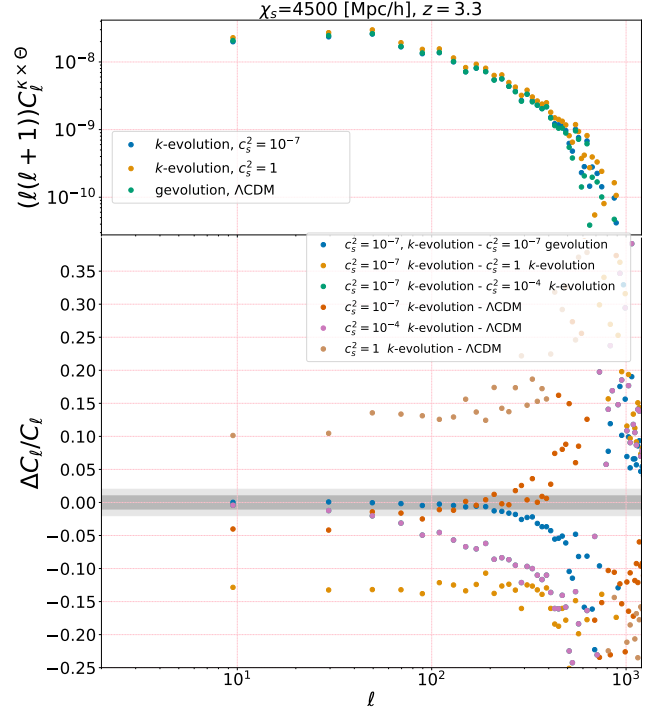


Figure 8. Same as Fig. 7, but for a source distance of $\chi_s = 4500$ Mpc/h, corresponding roughly to $z \approx 3.3$, and using N -body simulation data that covers $\sim 5\%$ of the sky.

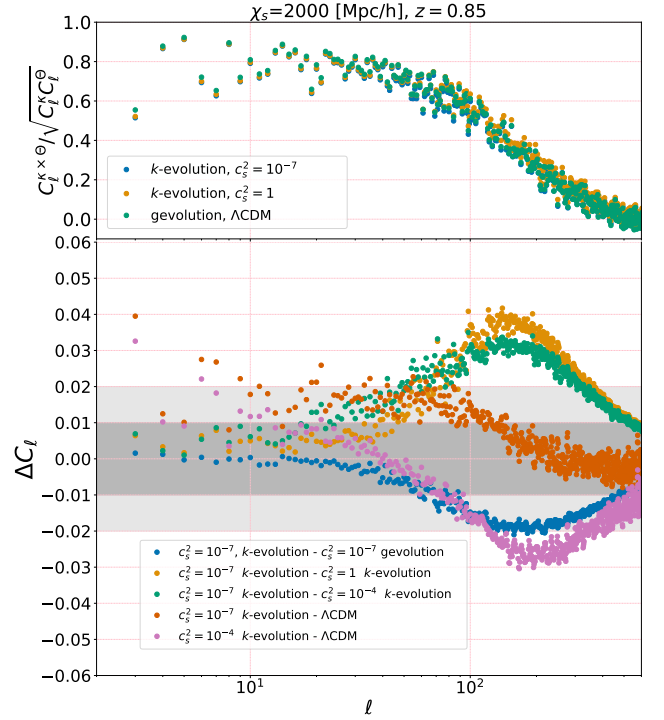


Figure 9. *Top panel:* The cross-correlation coefficient of lensing convergence κ and ISW-RS integrated to comoving distance $\chi_s = 2000$ Mpc/h for the results shown in Fig. 7. *Bottom panel:* Absolute difference in the cross-correlation coefficient for different models.

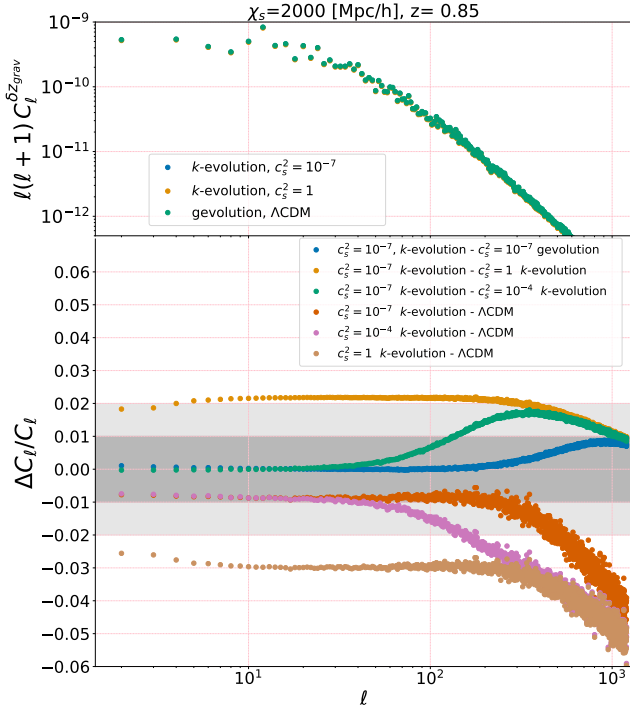


Figure 10. *Top panel:* The gravitational redshift angular power spectra of different cosmologies for a source plane at comoving distance $\chi_s = 2000$ Mpc/h. *Bottom panel:* The relative difference between the angular power spectra of the gravitational redshift in different cosmologies.

is only about 1%. Fig. 10 also shows that the effect of non-linear dark energy clustering becomes visible once again for $\ell \gtrsim 100$, and is generally rather small, of the order of 1%.

It should be noted that the angular correlation of the gravitational redshift will be very difficult to measure from large-scale structure observations. However, the line-of-sight correlations produce interesting signatures in redshift space, in particular a dipole in the correlation function of different matter tracers (Wojtak et al. 2011; Breton et al. 2019).

5.4 Shapiro time delay

In the Fig. 11 the angular power spectra for the Shapiro delay signal is plotted. Our result for the relative spectra show a similar pattern as for the gravitational redshift. The effect of dark energy clustering and dark energy background evolution have a $\sim 3\%$ effect on the Shapiro delay power spectrum that again cancel to a significant degree when combined. The non-linear dark energy clustering contributes again about a 1% effect for $\ell \gtrsim 100$. We only report the Shapiro delay integrating to $\chi_s = 2000$ Mpc/h. The cosmological Shapiro time delay will be extremely challenging to measure. It contributes only to subdominant relativistic corrections in the redshift-space clustering, and we are not aware of a probe that easily isolates this effect.

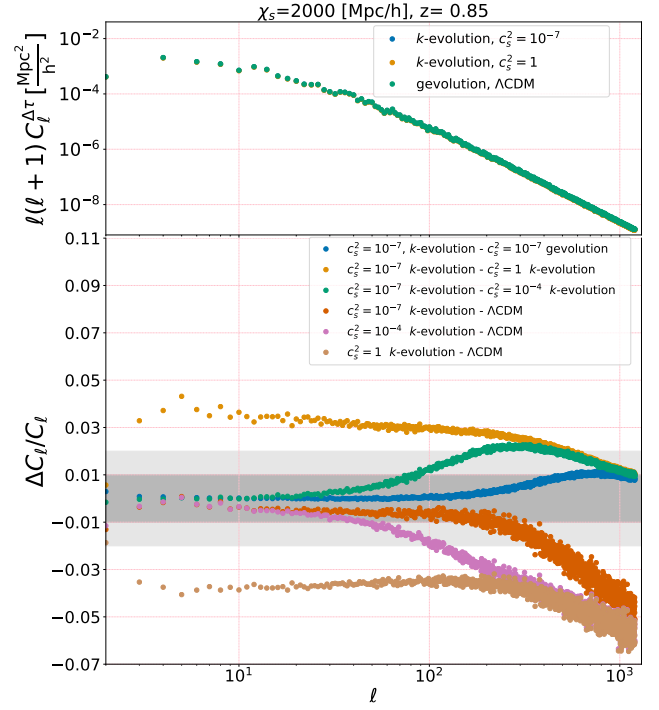


Figure 11. *Top panel:* The angular power spectra of Shapiro time delay integrated to comoving distance $\chi_s = 2000$ Mpc/h for different cosmologies. *Bottom panel:* The relative difference between Shapiro delay angular power spectra for different models.

6 CONCLUSION

We are, observationally speaking, in the golden era of cosmology and in the near future we will be able to put stringent constraints on dark energy and modified gravity models. However, to be able to unlock the full power of future observations we need to have a precise understanding of the non-standard scenarios well into the nonlinear regime. The precise modeling of structure formation and cosmological observables covering linear to nonlinear scales can be directly achieved using full N -body simulations.

In this work we have presented the numerical results for the effect of clustering dark energy (specifically the k -essence model) on the observables extracted from the gravitational potential, namely the weak gravitational lensing, ISW-RS, Shapiro time delay and gravitational redshift. The observables discussed in this paper are calculated via a ray-tracing method integrating to the source redshifts $z \approx 0.85$ and $z \approx 3.3$ covering respectively a full sky map and a pencil beam in our simulations. Comparing results from the two N -body codes *gevolution* and *k*-evolution with the linear Boltzmann code CLASS we are able to assess the different effects coming from the dark energy, specifically the effect from a different background evolution, from linear dark energy perturbations and from the non-linear evolution of dark energy itself.

In summary, our numerical analysis of the angular power spectra of each observable shows that:

- The ISW-RS signal is the most powerful probe of different background evolution and the clustering of dark en-

ergy. Comparing dark energy with various speeds of sound ($c_s^2 = 10^{-7}$, $c_s^2 = 10^{-4}$ and $c_s^2 = 1$) with Λ CDM one finds a significant impact of clustering dark energy on the ISW-RS angular power spectra reaching $\sim 35\%$ at $z = 3.3$ and $\sim 30\%$ at $z = 0.85$. Moreover, by comparing the linear ISW signal from CLASS with the non-linear signal from our N -body codes we are able to determine the scale and amplitude of the nonlinear Rees-Sciama effect in the k -essence scenario.

- The effect of dark energy on the weak gravitational lensing signal could reach $\sim 5\%$. Interestingly, our numerical study shows that the effect of clustering of dark energy and background evolution can partially cancel each other.

- The gravitational redshift and Shapiro time delay signals are less sensitive to the dark energy clustering and background evolution, as dark energy would change these signals at most by $\sim 3\%$ and $\sim 4\%$, respectively, due to the different background evolution. An additional change by $\sim 2\%$ and $\sim 3\%$ can occur due to the clustering of dark energy.

Our numerical study shows how direct probes of the gravitational field, in particular weak lensing and the ISW-RS effect, can be used to constrain the nature of dark energy. It also highlights the relevance of including non-linear effects and provides a framework to model these effects in full N -body simulations. With this we deliver some valuable guidance for the implementation of analysis pipelines that will be used to process the vast amount of upcoming observational data, with the aim to derive robust constraints on dark energy parameters.

ACKNOWLEDGEMENTS

FH would like to thank Francesca Lepori for helping in the maps analysis, Mona Jalilvand for helping in making linear angular power spectra and Shant Baghran for his comments about cross-correlating LSS data with ISW-RS signal. FH also would like to appreciate invaluable support from Jean-Pierre Eckmann during COVID-19 outbreak and his comments about our manuscript. FH and MK acknowledge funding from the Swiss National Science Foundation, and JA acknowledges funding by STFC Consolidated Grant ST/P000592/1. This work was supported by a grant from the Swiss National Supercomputing Centre (CSCS) under project ID s969. Part of the computations were performed at University of Geneva on the Baobab cluster.

Carbon footprint: Our simulations consumed about 9800 kWh of electrical energy, which is equivalent to 1960 kg CO₂ with a conversion factor of 0.2 kg CO₂ kWh⁻¹ from Vuarroz & Jusselme (2018), table 2, assuming Swiss mix.

DATA AVAILABILITY

The N -body codes used for the simulations and data of this paper will be provided upon request to the corresponding author. The version of *gevolution* used in this work, together with the map-making tools, is available on this public repository: <https://github.com/gevolution-code/gevolution-1.2>

APPENDIX A: CONVERGENCE TEST

In this appendix we compare the results from our high-resolution simulations ($N_{\text{grid}} = N_{\text{pcl}} = 4608^3$) with some lower-resolution ones ($N_{\text{grid}} = N_{\text{pcl}} = 2304^3$) for ISW-RS and convergence maps at both redshifts $z = 0.85$ and $z = 3.3$. This shows us at which scales the low-resolution simulations have converged to a certain numerical precision, and we can make a reasonable guess on how well we should be able to trust our final results from the high-resolution simulations.

According to Fig. A1 the convergence angular power spectrum is converged to within 5% up to $\ell \sim 100$ and $\ell \sim 250$, respectively for a source redshift of $z = 0.85$ and $z = 3.3$. Assuming that a factor of 2 in spatial resolution translates to a similar improvement in the angular resolution, we may want to trust our final results up to $\ell \sim 200$ and $\ell \sim 500$, respectively, maintaining a $\sim 5\%$ absolute convergence threshold. However, the leading-order error due to finite resolution is usually almost independent of cosmology, which means that it cancels out to high accuracy when taking ratios. Whenever we show relative changes, we therefore expect much better numerical convergence. In the bottom panel of the Fig. A1 we show the relative change between Λ CDM and w CDM convergence power spectra for two different spatial resolutions. In these relative spectra the curves with different resolutions agree at all ℓ shown, explicitly demonstrating the cancellation of the finite resolution error in the relative power spectra.

Considering Fig. A2 we can draw similar conclusions for the numerical convergence of the ISW-RS signal. The 5% error is reached at somewhat higher ℓ , which means we may be able to trust our final results up to $\ell \sim 400$ and $\ell \sim 800$ for the two redshift values if we apply the same requirement on absolute numerical convergence. Also according to the bottom panel of the figure the relative spectra from the two different resolutions are consistent so that we can trust the ISW-RS relative difference power spectra at all scales of interest. We emphasise again that the results shown in this paper were obtained using the higher-resolution simulations.

APPENDIX B: NON-LINEAR REES-SCIAMA EFFECT

In this appendix we quantify in more detail the contribution of the non-linear Rees-Sciama effect to the ISW-RS signal at low multipoles $\ell \lesssim 100$. To this end, we run additional simulations for the w CDM cosmology with $c_s^2 = 1$ and for Λ CDM, but with the power of primordial perturbations, A_s , reduced by two orders of magnitude. As a result, the evolution is almost linear up to much smaller scales, bringing the numerical result for the ISW-RS signal into very good agreement with the calculation of the linear ISW alone as performed by CLASS. This can be clearly seen in the left panel of Fig. B1 where the simulations with low A_s remain consistent with the prediction from CLASS well beyond $\ell \sim 100$. Taking the ratio of spectra from the simulations with the standard value of A_s to the ones with low A_s , we can therefore get a good estimate of the fractional contribution of the Rees-Sciama effect. The result of this analysis is shown in the right panel of Fig. B1, which suggests that the Rees-Sciama effect

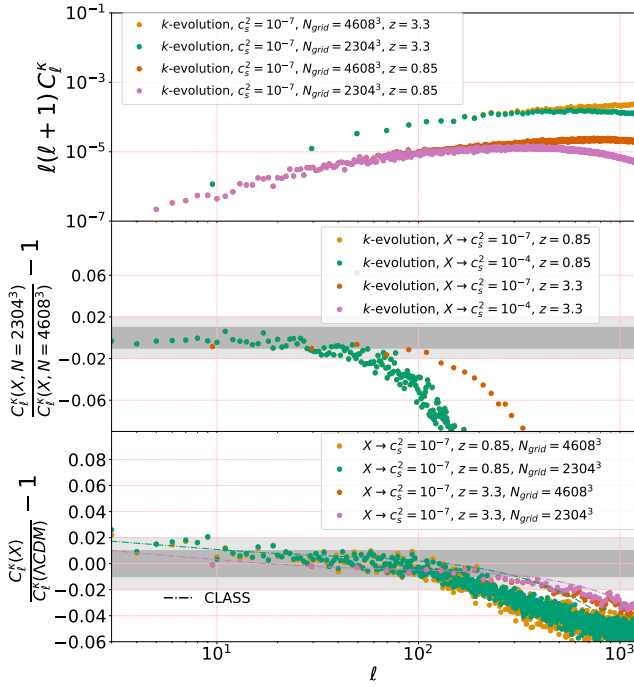


Figure A1. Top panel: We compare the convergence power spectra from two simulations with different resolutions, $N_{\text{grid}} = N_{\text{pcl}} = 4608^3$ and $N_{\text{grid}} = N_{\text{pcl}} = 2304^3$, at two source redshifts $z = 0.85$ and $z = 3.3$. **Middle panel:** The relative difference between the convergence power spectra of the same cosmology but different resolutions of the simulations are shown. This gives us an estimation of the finite resolution error on the convergence angular power spectra. The grey areas show 1% and 2% numerical agreement. **Bottom panel:** Comparing the relative change in the convergence power spectra between ΛCDM and k -essence cosmology with the speed of sound $c_s^2 = 10^{-7}$ from two simulations with different resolutions, $N_{\text{grid}} = N_{\text{pcl}} = 4608^3$ and $N_{\text{grid}} = N_{\text{pcl}} = 2304^3$, at source redshifts $z = 0.85$ and $z = 3.3$. The dashed lines show the linear theory prediction obtained from CLASS. The agreement across different resolutions shows that one can trust the relative change of power spectra at much higher multipoles than is the case for the individual power spectra themselves.

changes the signal by a few per cent at very low $\ell \lesssim 20$, and then gradually ramps up to reach a $\sim 100\%$ correction at around $\ell \sim 100$. Interestingly, the non-linear corrections are systematically larger in ΛCDM , which can be explained by the fact that the linear growth rate is slightly suppressed in our $w\text{CDM}$ cosmology, see Fig. 1. This, in turn, is expected to lead to a corresponding relative suppression of second-order corrections like the Rees-Sciama effect.

REFERENCES

- Abate A., et al., 2012, preprint ([arXiv:1211.0310](#))
 Adamek J., Daverio D., Durrer R., Kunz M., 2016a, *JCAP*, 07, 053
 Adamek J., Daverio D., Durrer R., Kunz M., 2016b, *Nature Phys.*, 12, 346
 Adamek J., Durrer R., Kunz M., 2017a, *JCAP*, 11, 004
 Adamek J., Brandbyge J., Fidler C., Hannestad S., Rampf C., Tram T., 2017b, *Mon. Not. Roy. Astron. Soc.*, 470, 303

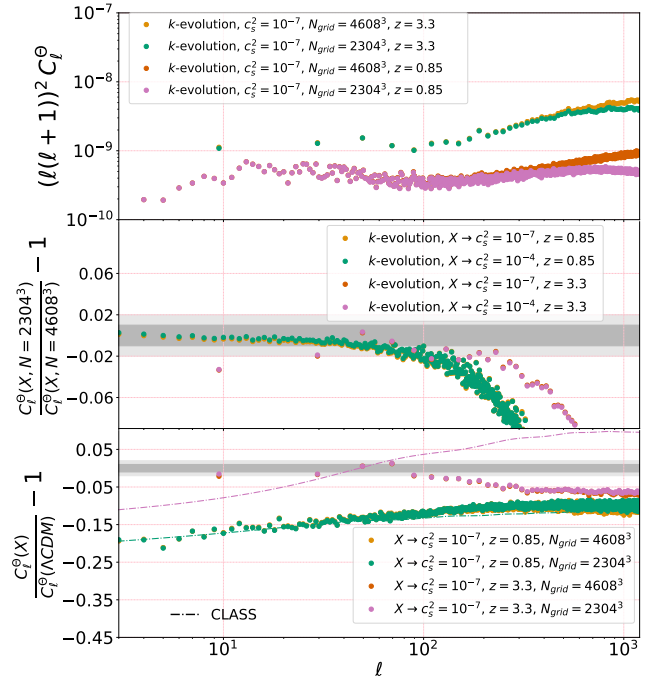


Figure A2. Top panel: We compare the ISW-RS angular power spectra from two simulations with different resolution, $N_{\text{grid}} = N_{\text{pcl}} = 4608^3$ and $N_{\text{grid}} = N_{\text{pcl}} = 2304^3$, at two source redshifts $z = 0.85$ and $z = 3.3$. **Middle panel:** The relative difference between the ISW-RS angular power spectra of the same cosmology but different resolutions of the simulations are shown. **Bottom panel:** The relative difference of ISW-RS angular power spectra between the k -essence cosmology with $c_s^2 = 10^{-7}$ and ΛCDM for two different spatial resolutions $N_{\text{grid}} = N_{\text{pcl}} = 4608^3$ and $N_{\text{grid}} = N_{\text{pcl}} = 2304^3$ at two source redshifts $z = 0.85$ and $z = 3.3$. The dashed lines show the linear theory prediction obtained from CLASS. Like Fig. A1, this figure shows that the finite resolution effect is cancelled significantly in the relative changes of the angular power spectra.

- Adamek J., Clarkson C., Coates L., Durrer R., Kunz M., 2019, *Phys. Rev. D*, 100, 021301
 Adamek J., Rasera Y., Corasaniti P. S., Alimi J.-M., 2020, *Phys. Rev. D*, 101, 023512
 Ade P., et al., 2014a, *Astron. Astrophys.*, 571, A17
 Ade P., et al., 2014b, *Astron. Astrophys.*, 571, A19
 Ade P., et al., 2016a, *Astron. Astrophys.*, 594, A13
 Ade P., et al., 2016b, *Astron. Astrophys.*, 594, A14
 Ade P., et al., 2016c, *Astron. Astrophys.*, 594, A21
 Aghamousa A., et al., 2016, preprint ([arXiv:1611.00036](#))
 Alam S., Zhu H., Croft R. A. C., Ho S., Giusarma E., Schneider D. P., 2017, *Mon. Not. Roy. Astron. Soc.*, 470, 2822
 Alsing J., Kirk D., Heavens A., Jaffe A., 2015, *Mon. Not. Roy. Astron. Soc.*, 452, 1202
 Amendola L., Kunz M., Sapone D., 2008, *JCAP*, 04, 013
 Amendola L., et al., 2018, *Living Rev. Rel.*, 21, 2
 Armendariz-Picon C., Mukhanov V. F., Steinhardt P. J., 2000, *Phys. Rev. Lett.*, 85, 4438
 Armendariz-Picon C., Mukhanov V. F., Steinhardt P. J., 2001, *Phys. Rev. D*, 63, 103510
 Aubourg É., et al., 2015, *Phys. Rev. D*, 92, 123516
 Bacon D. J., Refregier A. R., Ellis R. S., 2000, *Mon. Not. Roy. Astron. Soc.*, 318, 625
 Baldi M., 2012, *Phys. Dark Univ.*, 1, 162
 Barreira A., Li B., Hellwing W. A., Baugh C. M., Pascoli S., 2013,

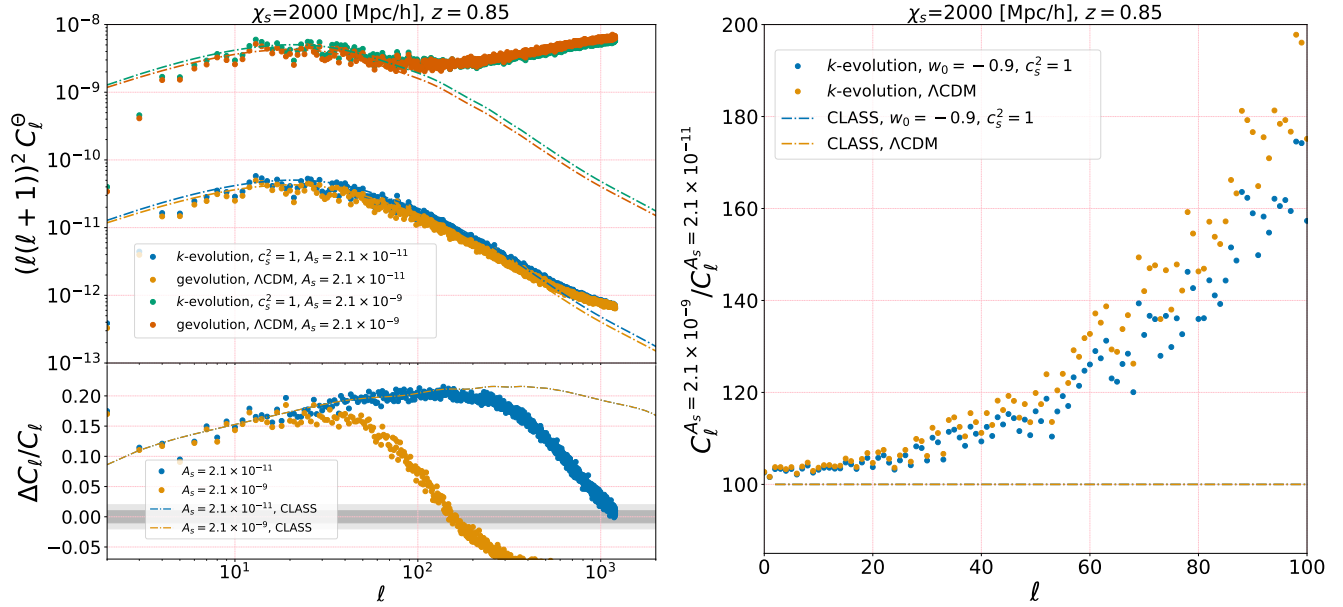


Figure B1. *Left:* The ISW-RS angular power spectra for two different cosmologies, ($w_0 = -0.9$, $c_s^2 = 1$) and Λ CDM with standard and low value of A_s , the amplitude of scalar perturbations. *Right:* The ratio of the ISW-RS signal from high value of A_s to low value of A_s are compared. The linear result is constant at all scales, and is simply the ratio of the two values of A_s . The fractional contribution of the Rees-Sciama effect depends on w_0 mainly because of suppressed growth and the corresponding shift of the non-linear scale with respect to Λ CDM.

- JCAP, 10, 027
- Bartelmann M., Schneider P., 2001, *Phys. Rept.*, 340, 291
- Beck R., Csabai I., R  acz G., Szapudi I., 2018, *Mon. Not. Roy. Astron. Soc.*, 479, 3582
- Becker M. R., 2013, *Mon. Not. Roy. Astron. Soc.*, 435, 115
- Bellini E., Sawicki I., 2014, *JCAP*, 07, 050
- Blanchard A., et al., 2019, preprint ([arXiv:1910.09273](https://arxiv.org/abs/1910.09273))
- Blas D., Lesgourgues J., Tram T., 2011, *JCAP*, 07, 034
- Bonvin C., Durrer R., 2011, *Phys. Rev. D*, 84, 063505
- Brandbyge J., Hannestad S., 2009, *JCAP*, 05, 002
- Brando G., Koyama K., Wands D., 2020, preprint ([arXiv:2006.11019](https://arxiv.org/abs/2006.11019))
- Brax P., Davis A.-C., Li B., Winther H. A., Zhao G.-B., 2012, *JCAP*, 10, 002
- Breton M.-A., Rasera Y., Taruya A., Lacombe O., Saga S., 2019, *Mon. Not. Roy. Astron. Soc.*, 483, 2671
- Broadhurst T. J., Scannapieco E., 2000, *Astrophys. J. Lett.*, 533, L93
- Cabass G., Gerbino M., Giusarma E., Melchiorri A., Pagano L., Salvati L., 2015, *Phys. Rev. D*, 92, 063534
- Cai Y.-C., Cole S., Jenkins A., Frenk C., 2009, *Mon. Not. Roy. Astron. Soc.*, 396, 772
- Cai Y.-C., Cole S., Jenkins A., Frenk C. S., 2010, *Mon. Not. Roy. Astron. Soc.*, 407, 201
- Cai Y.-C., Li B., Cole S., Frenk C. S., Neyrinck M., 2014, *Mon. Not. Roy. Astron. Soc.*, 439, 2978
- Cai Y.-C., Neyrinck M., Mao Q., Peacock J. A., Szapudi I., Berlind A. A., 2017, *Mon. Not. Roy. Astron. Soc.*, 466, 3364
- Cappi A., 1995, *A&A*, 301, 6
- Carbone C., Petkova M., Dolag K., 2016, *JCAP*, 07, 034
- Challinor A., Lewis A., 2011, *Phys. Rev. D*, 84, 043516
- Clifton T., Ferreira P. G., Padilla A., Skordis C., 2012, *Phys. Rept.*, 513, 1
- Creminelli P., D'Amico G., Norena J., Vernizzi F., 2009, *JCAP*, 02, 018
- Dakin J., Hannestad S., Tram T., Knabenhans M., Stadel J., 2019, *JCAP*, 08, 013
- Dossett J., Ishak M., 2013, *Phys. Rev. D*, 88, 103008
- Durrer R., 2001, *J. Phys. Stud.*, 5, 177
- Francis C., Peacock J., 2010, *Mon. Not. Roy. Astron. Soc.*, 406, 2
- Gleyzes J., Langlois D., Piazza F., Vernizzi F., 2013, *JCAP*, 08, 025
- Gorski K., Hivon E., Banday A., Wandelt B., Hansen F., Reinecke M., Bartelman M., 2005, *Astrophys. J.*, 622, 759
- Granett B. R., Neyrinck M. C., Szapudi I., 2008, *Astrophys. J. Lett.*, 683, L99
- Gubitosi G., Piazza F., Vernizzi F., 2013, *JCAP*, 02, 032
- Handley W., Lemos P., 2019, *Phys. Rev. D*, 100, 043504
- Hannestad S., Tu H., Wong Y. Y., 2006, *JCAP*, 06, 025
- Hansen S. H., Hassani F., Lombriser L., Kunz M., 2020, *JCAP*, 01, 048
- Hassani F., Lombriser L., 2020, preprint ([arXiv:2003.05927](https://arxiv.org/abs/2003.05927))
- Hassani F., Baghran S., Firouzjahi H., 2016, *JCAP*, 05, 044
- Hassani F., Adamek J., Kunz M., Vernizzi F., 2019, *JCAP*, 12, 011
- Hassani F., L'Huillier B., Shafieloo A., Kunz M., Adamek J., 2020, *JCAP*, 04, 039
- Hikage C., et al., 2019, *Publ. Astron. Soc. Jap.*, 71, Publications of the Astronomical Society of Japan, Volume 71, Issue 2, April 2019, 43, <https://doi.org/10.1093/pasj/psz010>
- Hu W., Cooray A., 2001, *Phys. Rev. D*, 63, 023504
- Jain B., Taylor A., 2003, *Phys. Rev. Lett.*, 91, 141302
- Jimeno P., Broadhurst T., Coupon J., Umetsu K., Lazkoz R., 2015, *Mon. Not. Roy. Astron. Soc.*, 448, 1999
- Joyce A., Lombriser L., Schmidt F., 2016, *Ann. Rev. Nucl. Part. Sci.*, 66, 95
- Khosravi S., Mollazadeh A., Baghran S., 2016, *JCAP*, 09, 003
- Kim Y.-R., Croft R. A., 2004, *Astrophys. J.*, 607, 164
- Koyama K., 2018, *Int. J. Mod. Phys. D*, 27, 1848001
- Kunz M., Sapone D., 2007, *Phys. Rev. Lett.*, 98, 121301
- K  hlinger F., et al., 2017, *Mon. Not. Roy. Astron. Soc.*, 471, 4412
- Laureijs R., et al., 2011, preprint ([arXiv:1110.3193](https://arxiv.org/abs/1110.3193))
- Lepori F., Adamek J., Durrer R., Clarkson C., Coates L., 2020,

- preprint ([arXiv:2002.04024](#))
- Lewis A., Challinor A., 2006, *Phys. Rept.*, 429, 1
- Li B., Zhao G.-B., Teyssier R., Koyama K., 2012, *JCAP*, 01, 051
- Li B., Barreira A., Baugh C. M., Hellwing W. A., Koyama K., Pascoli S., Zhao G.-B., 2013, *JCAP*, 11, 012
- Li P., Dodelson S., Hu W., 2019, *Phys. Rev. D*, 100, 043502
- Llinares C., Mota D. F., Winther H. A., 2014, *Astron. Astrophys.*, 562, A78
- Mandelbaum R., 2018, *Ann. Rev. Astron. Astrophys.*, 56, 393
- Martin J., 2012, *Comptes Rendus Physique*, 13, 566
- Mead A., Peacock J., Heymans C., Joudaki S., Heavens A., 2015, *Mon. Not. Roy. Astron. Soc.*, 454, 1958
- Nusser A., 2016, *Astrophys. J. Lett.*, 821, L2
- Oyaizu H., Lima M., Hu W., 2008, *Phys. Rev. D*, 78, 123524
- Peiris H. V., Spergel D. N., 2000, *Astrophys. J.*, 540, 605
- Percival W. J., Cole S., Eisenstein D. J., Nichol R. C., Peacock J. A., Pope A. C., Szalay A. S., 2007, *Mon. Not. Roy. Astron. Soc.*, 381, 1053
- Perlmutter S., et al., 1999, *Astrophys. J.*, 517, 565
- Pratten G., Lewis A., 2016, *JCAP*, 08, 047
- Puchwein E., Baldi M., Springel V., 2013, *Mon. Not. Roy. Astron. Soc.*, 436, 348
- Rees M., Sciama D., 1968, *Nature*, 217, 511
- Refregier A., 2003, *Ann. Rev. Astron. Astrophys.*, 41, 645
- Reverberi L., Daverio D., 2019, *JCAP*, 07, 035
- Riess A. G., et al., 1998, *Astron. J.*, 116, 1009
- Sachs R., Wolfe A., 1967, *Astrophys. J.*, 147, 73
- Sadeh I., Feng L. L., Lahav O., 2015, *Phys. Rev. Lett.*, 114, 071103
- Santos M. G., et al., 2015, *PoS*, AASKA14, 019
- Schmidt F., Lima M. V., Oyaizu H., Hu W., 2009, *Phys. Rev. D*, 79, 083518
- Schmidt F., Leauthaud A., Massey R., Rhodes J., George M. R., Koekemoer A. M., Finoguenov A., Tanaka M., 2012, *Astrophys. J. Lett.*, 744, L22
- Scranton R., et al., 2003, preprint ([arXiv:astro-ph/0307335](#))
- Seljak U., 1996, *Astrophys. J.*, 460, 549
- Shapiro I. I., 1964, *Phys. Rev. Lett.*, 13, 789
- Spergel D., et al., 2003, *Astrophys. J. Suppl.*, 148, 175
- Spurio Mancini A., Reischke R., Pettorino V., SchÄd'fer B., ZumalacÄarregui M., 2018, *Mon. Not. Roy. Astron. Soc.*, 480, 3725
- Szapudi I., Prunet S., Pogosyan D., Szalay A. S., Bond J., 2000, preprint ([arXiv:astro-ph/0010256](#))
- Takahashi R., Sato M., Nishimichi T., Taruya A., Oguri M., 2012, *Astrophys. J.*, 761, 152
- Takahashi R., Hamana T., Shirasaki M., Namikawa T., Nishimichi T., Osato K., Shiroshima K., 2017, *Astrophys. J.*, 850, 24
- Tegmark M., et al., 2004, *Phys. Rev. D*, 69, 103501
- Tegmark M., et al., 2006, *Phys. Rev. D*, 74, 123507
- Valogiannis G., Bean R., 2017, *Phys. Rev. D*, 95, 103515
- Verde L., Treu T., Riess A. G., 2019, *Nature Astronomy*, 3, 891
- Vuarnoz D., Jusselme T., 2018, *Energy*, 161, 573
- Wandelt B. D., Hivon E., Gorski K. M., 2001, *Phys. Rev. D*, 64, 083003
- Wojtak R., Hansen S. H., Hjorth J., 2011, *Nature*, 477, 567
- Wyman M., Jennings E., Lima M., 2013, *Phys. Rev. D*, 88, 084029
- Yoo J., Fitzpatrick A., Zaldarriaga M., 2009, *Phys. Rev. D*, 80, 083514
- Zhao G.-B., Li B., Koyama K., 2011, *Phys. Rev. D*, 83, 044007
- Zhu H., Alam S., Croft R. A., Ho S., Giusarma E., Leauthaud A., Merrifield M., 2019, preprint ([arXiv:1901.05616](#))
- van Waerbeke L., et al., 2000, *Astron. Astrophys.*, 358, 30